ETH *zürich*

Reconstructing a 3D model from geophysical data for local amplification modelling: The study case of the upper Rhone valley, Switzerland

Journal Article

Author(s):
Panzera, Francesco (iD); Alber, Jonas; Imperatori, Walter; Bergamo, Paolo; Fäh, Donat
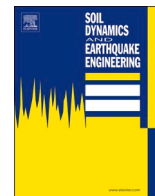
Reconstructing a 3D model from geophysical data for local amplification modelling: The study case of the upper Rhone valley, Switzerland

Francesco Panzera [*], Jonas Alber, Walter Imperatori, Paolo Bergamo, Donat Fäh

Swiss Seismological Service, ETH Zurich, Switzerland

ARTICLE INFO

ABSTRACT

The geometry of three-dimensional subsurface structures plays an important role in determining local seismic site effects as in the case of alpine valleys. Detailed knowledge of these structures is fundamental in seismic hazard and risk studies. In this study we investigate an area in the upper Rhone valley around Visp, in the southwestern part of Switzerland. A large dataset of geological and geophysical data, consisting of borehole logs, microtremor horizontal to vertical spectral ratios and shear-wave velocity measurements, was compiled to build a detailed 3D model of the subsurface. By combining fundamental frequency information from noise recordings and shear-wave velocity profiles, three main geophysical discontinuities were identified and their physical properties constrained through a stepwise process. First, the bedrock depth was estimated; in a second step a generic velocity model was defined and finally, combining all the available geological and geophysical information, we developed a 3D geophysical model. The model was compared with a local 3D geological model and a model derived from gravimetric data. The study area is a complex alpine valley where 2D/3D wave propagation phenomena occur. In such case a purely 1D response assumption is considered to be invalid. In order to test the 3D model, we modelled different ambient-vibration wave fields and compared observed and synthetic H/V spectral ratios. We slightly modified our 3D geophysical model in some areas based on this comparison. Finally, a good match between simulated and empirical spectral ratios corroborated the model. The results suggest that the use of ambient vibration techniques are a powerful and cost-effective tools to reconstruct three-dimensional models of the subsurface. Finally, we used the 3D model to predict amplification of earthquake ground motion in the basin. Again, the match between observed and modelled amplification at the locations of the seismic stations is good. This allows us to map amplification inside the study area.

1. Introduction

The Rhone valley in the South-Western part of Switzerland (see inset in Fig. 1) is located in the most active seismic zones of the country [1]. This area was struck by a series of strong seismic events such as the 1755 Brig (Mw 5.7), the 1855 Visp (Mw 6.2) and the 1946 Sierre (Mw 5.8) earthquakes ([2,3]. The shape of the valley and the high velocity contrast between sediments and bedrock make this area susceptible to 2D/3D seismic site amplification effects [4–9]. Due to the ongoing urban development, the Rhone valley is an area of particular interest to study site amplification effects. For this purpose, a detailed knowledge of the geometry, thickness and velocity of the main sedimentary layers in the valley is required. Previous studies have shown that such 3D structures play an important role in seismic wave propagation and amplification (e. g. Refs. [10–12]. In particular, several authors have successfully

modelled, with numerical simulations, the amplification in a 3D basin setting [13–15]. Among these for the Rhone valley area Roten et al. [6] developed a 3D geophysical model for the city of Sion in the central Swiss Rhone valley, and successfully compared simulated earthquake ground motion with observations. They quantified the effects of 2D/3D resonances and edge-generated surface waves on the ground motion amplification.

The geometry and the structure of the subsoil can be effectively investigated using several non-invasive techniques, such as ambient vibration surveys based on single station and/or seismic array measurements (e.g. Refs. [18–21]. In particular, the horizontal to vertical spectral ratio (HVSR) method is useful to retrieve the fundamental frequency (f_0) of soft sediment (e.g. Ref. [22], whereas seismic array processing techniques as the *f-k* analysis can be used to estimate S-wave velocity (V_S) profiles of the subsurface (e.g. Ref. [23]. f_0 and V_S profile

---

are key parameters to estimate the thickness (H) of the soft sediments overlying the bedrock (e.g. Refs. [24,25]. The thickness obtained by combining f_0 and V_S is in most cases in good agreement with estimates obtained with other geophysical techniques such as gravimetry (e.g. Ref. [26] as long as the investigated structure is not too complex. In fact, several authors (e.g. Refs. [27,28] have warned that f_0 must carefully interpreted, since even in the same geological formation different peaks can be observed. Furthermore, sometimes a peak can simply not be easily seen or when it exists, it does not correspond to the actual resonant frequency.

In the framework of the Earthquake Risk Model Switzerland project (ERM-CH, http://www.seismo.ethz.ch/en/research-and-teaching/ongoing-projects/), the area around the municipality of Visp, located in the upper Rhone valley, was selected to build a detailed 3D geophysical model and to develop models for site amplification. We used a large set of geophysical data, either collected in the past during the COGEAR project [29] or more recently within the ERM-CH project [30,31]. For the area of Visp (Fig. 1), the Swiss Seismological Service (SED) database (http://stations.seismo.ethz.ch) contains 487 single-station noise measurements, 12 small aperture seismic arrays (of which only 10 inside the basin were used), 2 MASW and 98 borehole logs from geocadast repository (https://geocadast.crealp.ch).

These data were used in a stepwise process in which HVSR and borehole data helped to constrain the bedrock depth, whereas velocity profiles obtained from surface waves dispersion curve inversions were used to derive a velocity model. Therefore, we combined all the available geological and geophysical information to constrain the subsoil structure. The obtained model was compared with a model based on gravimetric data available for the Rhone valley, and a local 3D geological model established for Visp by Canton Valais and Swisstopo.

Several temporary and permanent seismic stations were operated in the past decades, and are used to verify modelled ground-motion amplification.

2. Geological setting

The study area is shown in Fig. 1 centered around the municipality of Visp and extending for about 3 and 6 km along the N–S and E-W directions, respectively. The valley, which hosted the Rhone glacier, is crossed by the homonymous river in the E-W direction. Depending on the position along the valley, the bedrock is composed by Penninic units, mainly outcropping in the south-western part, or by Helvetic units, exposed towards the northern side [32]. These rocks, originating from continental and lithosphere deformation [33], are calcareous metasedimentary rocks (Penninic units) and gneisses, granites or schists (Helvetic units). From a tectonic point of view, the two bedrock formations are controlled by the Rhone-Simplon fault, a strike-slip fault striking along the Rhone valley [34]. The shape of the bedrock was derived in the past based on seismic reflection [35,36] and gravimetric profiles [37]. The Quaternary infill of the valley is represented by a complex succession of alluvial, glaciolacustrine and moraine deposits, locally overlapped by landslide material and detritus from the valley edges. The alluvial deposits can be subdivided into upper and lower units, where the former are mainly silt linked to flooding episodes and the latter are composed of gravel and sand from the river bed. The glaciolacustrine deposits are instead a complex succession of bedload sediments, gravel and sand, and suspended load sediments, mainly silt and clay. Finally, the moraine deposits represent the deepest layer made by rock detritus carried by the glacier [35,36,38,39]. This subdivision of the Quaternary deposits is confirmed by the recent 3D geological model
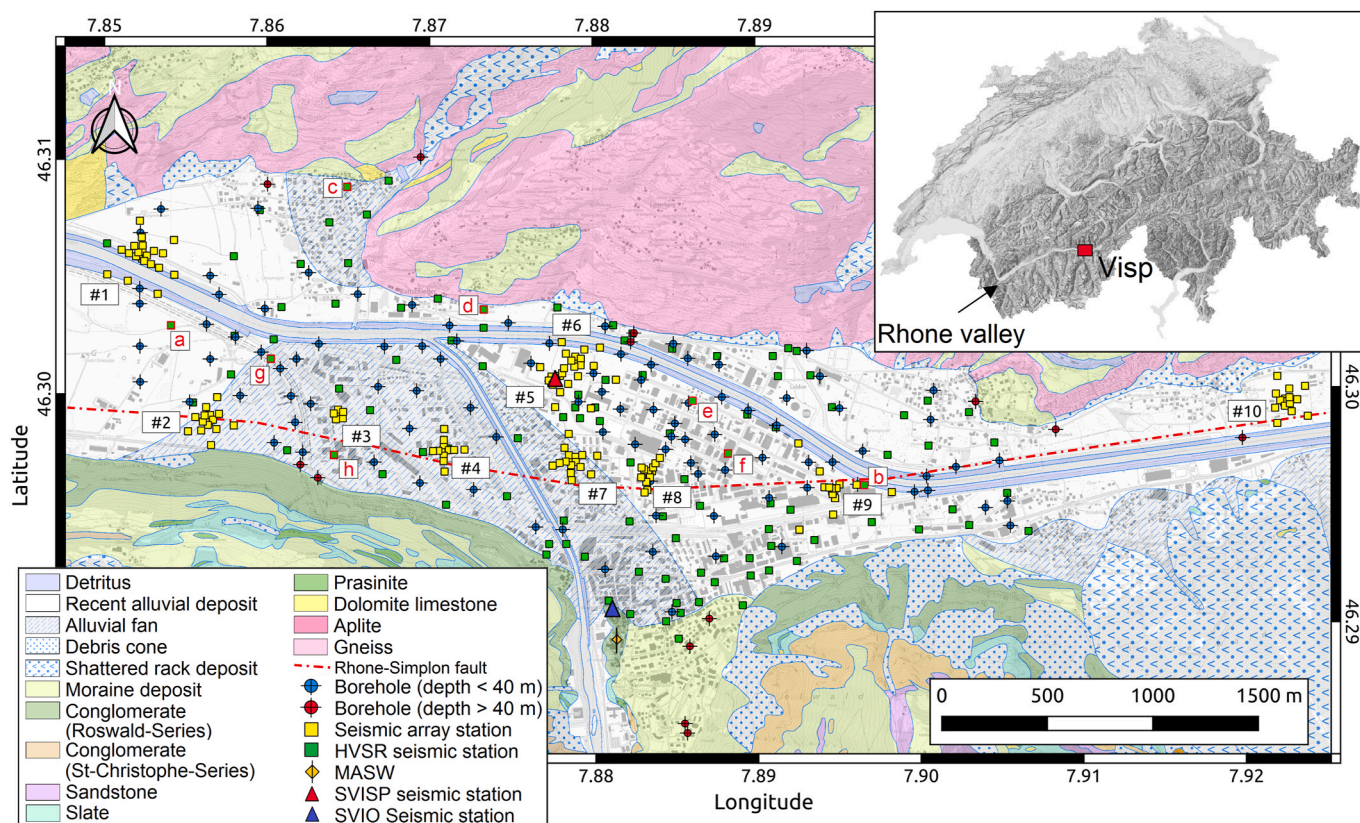

Fig. 1. Geological map of the investigated area (modified from Ref. [16] - geocover V3 map of Raron CN 1288). The red line in the geological map shows the rough location of the Rhone-Simplon fault inside the valley (modified from Ref. [17] – GK500). The inset map in the upper right corner shows the study area location in Switzerland. The green rectangles with red borders and the corresponding letters show the locations of selected HVSRs displayed in Fig. 2 (a, b, c and d) and in Fig. 11 (e, f, g and h). The maps are plotted with the permission of Swisstopo JA100120.

for the Visp area, produced by the Federal Office of Topography (Swisstopo) in collaboration with the Environment department of the Canton Valais. The model is mainly based on information coming from surficial boreholes (depth generally lower than 30 m) and its main purpose is for hydrogeological modelling. This model was developed in the framework of the project GeoQuat that aims in collecting and reviewing all the different sources of information related to Quaternary deposits in Switzerland [40].

3. Geophysical data processing

3.1. HVSR processing and picking

The 487 single-station ambient vibration measurements (green rectangles in Fig. 1) were processed by means of the HVSR technique, which is considered a fast method to support microzonation studies (e.g. Refs. [41,42], showing generally a peak corresponding to the fundamental frequency of resonance f_0 of the site (e.g. Ref. [43]. The measurements were performed in different projects over the past decades [21,44–46] using different sensors and dataloggers. For this reason, all the available measurements in the SED database (http://stations.seismo.ethz.ch) from these projects were included in our study. Finally, we selected 200 measurements having a sampling rate of 200 Hz and a recording duration of at least 40 min. All are from measurements with 3-component 5s velocimeters. The recorded signals were homogenously

reprocessed to obtain Fourier spectra in the frequency range 0.2–20 Hz, by subdividing it in 50 s time windows. The window length was set equal to 10 times the minimum processed signal period (T = 1/f). A Konno and Ohmachi [47] smoothing filter was applied to the spectra, with the *b* parameter set to 40. For each time window, the horizontal components quadratic mean was divided by the vertical component. The final spectral ratio for each investigated site was calculated by taking the average of the logarithmic HVSRs obtained from all the time windows [48]. When possible, the f_0 was picked on the 200 HVSR curves and mapped (Fig. 2). Moreover, in compliance with SESAME [48] criteria, we verified the peak amplitude and frequency stability of the picked f_0.

3.2. Processing and inversion of surface wave data from array acquisitions

As anticipated, 10 small-aperture 2D seismic arrays (see location in Fig. 1) had been deployed over time in the valley basin, recording ambient seismic vibrations [21,45,46]. Each seismic array was deployed with 12–16 stations (Lennartz 5s sensors). The original data were homogeneously reprocessed with the 3 component high resolution f-k method of Poggi and Fäh [23]; providing Love and Rayleigh wave dispersion curves and Rayleigh wave ellipticity. In addition, we used the RayDec technique [49] to extract Rayleigh wave ellipticity curves at each measurement point of the arrays. Examples of seismic arrays geometry used and achieved results are shown in Fig. 3.
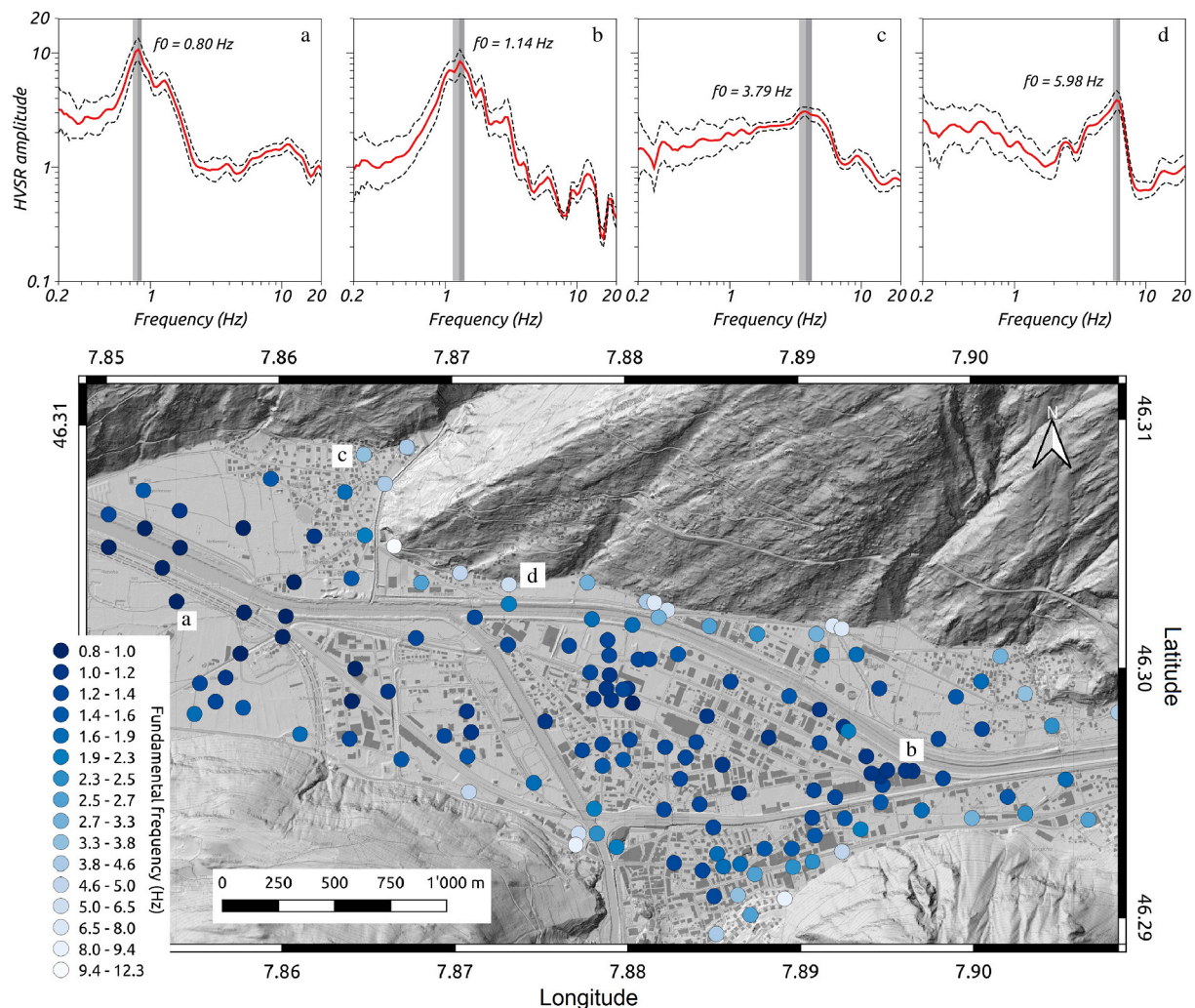

Fig. 2. Examples of HVSR curves and picked f_0 peak. The sites (with the corresponding letters) are shown in this map and also in Fig. 1. The map shows the f_0 peak geographic distribution inside the valley.
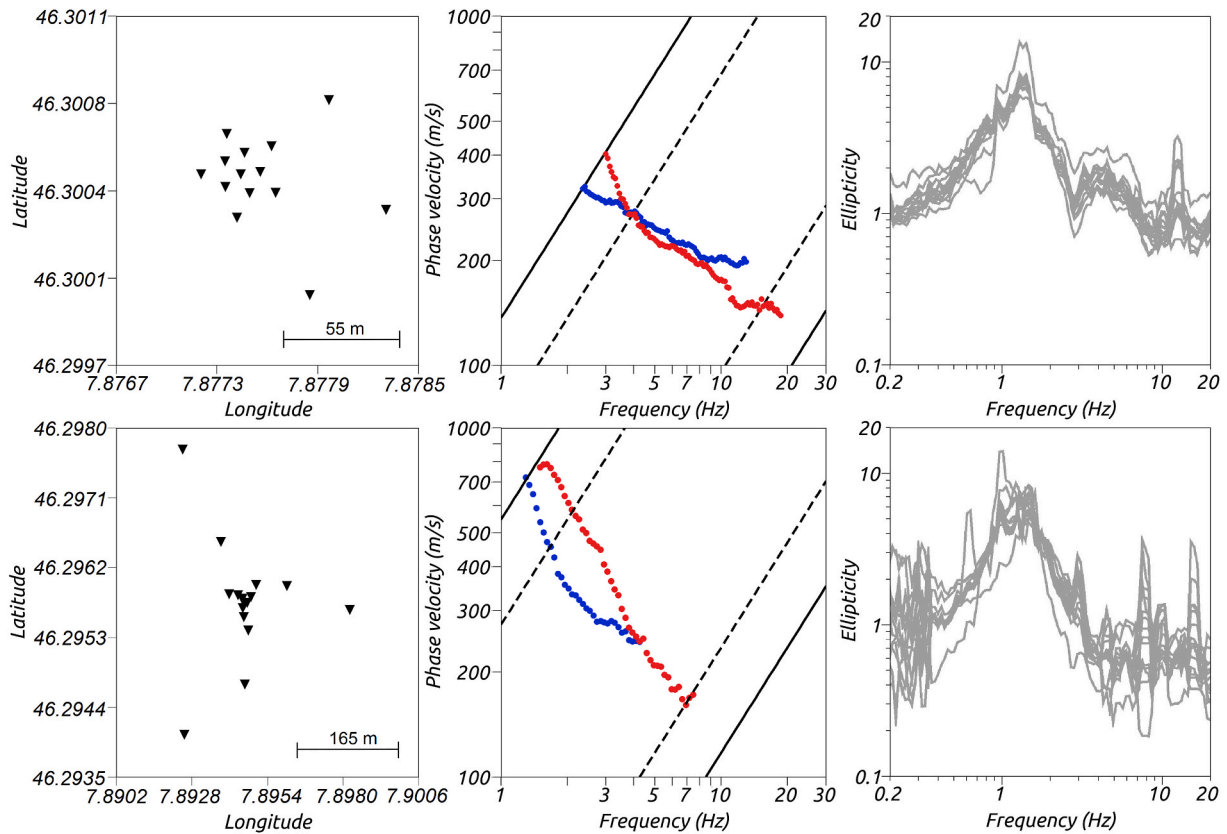
Fig. 3. From left to right examples for the seismic arrays #5, upper row, and #10, lower row, (see location in Fig. 1), Love (blue dots) and Rayleigh (red dots) dispersion curves with array limits (black lines) and RayDec ellipticity at each station site (grey lines). Continuous and dashed black lines in the DC graphs show the array resolution.

Love and Rayleigh wave dispersion curves and Rayleigh wave ellipticity were inverted together to estimate the V_S profiles below each seismic array. Note that in 8 cases over 10 the computed dispersion curves did not present a frequency coverage that could be used to retrieve the velocity contrast at the bedrock interface. By adding to the inversion, the low-frequency Rayleigh wave ellipticity extracted from single-station data at the array center, we constrained the velocity profile down to the bedrock interface. In fact, it is well known that the joint use of ellipticity, fundamental frequency and dispersion curve increases the investigation depth [21,50–52]. The inversion was carried out using the dinver code [53], considering for all the sites parameterizations of 4–8 constant-velocity layers having V_P, V_S, Poisson ratio and density in the range 200–5000 m/s, 50–3500 m/s, 0.2–0.5 and 1700–2300 kg/m^3, respectively. Note that density of the bedrock was set to 2700 kg/m^3. The chosen density values for sedimentary cover and bedrock used in the inversion are based on Rosselli [54]. Examples of inversions are given in Fig. 4.

The selected V_S profiles (Fig. 5) for all the seismic arrays have a 5 layers parameterization; the results indicate only a weak velocity contrast between the first and the second layer (total thickness of the first two layers is between 1 and 11 m and is not well resolved in Fig. 5 plots). In Fig. S1 of the supplementary material, the V_S profiles are compared to previous analysis (taken from the SED database). The comparison clearly shows that the surficial part of the profiles are similar, whereas by using ellipticity information the deeper parts of the velocity profiles are better resolved in our analysis.

Besides the microtremor array measurements carried out, an active surface wave survey (MASW) was performed in Visp (see location in Fig. 1) on calcareous metasedimentary rock [55]. The available space was not enough to deploy a long linear array and, consequently, 14 seismic stations with a 2 m inter-station distance were used, resulting in

a total line length of 26 m. Each recorder (24 bit datalogger Quanterra Q330) was equipped with two three components Lennartz 3C 5s sensor. Seismic waves were excited by a 120 kg mass dropped from a height of 1 m and located 10 m away from the first sensor. The *f-k* spectra of ten single shots were stacked to improve the signal-to-noise ratio of the final dispersion curves. For their inversion we used same code and parametrization as for the passive seismic array, but the obtained best-fitting model is characterized by 6 layers (Fig. 6). The surficial part of the bedrock profile in Visp is characterized by a 2 m thick detritus with V_S lower than 400 m/s, followed by a gradual increase from 800 m/s to 1200 m/s. The rock at the surface has a V_S of about 1000 m/s, progressively increasing with depth.

4. Definition of the 3D geophysical model

4.1. Velocity model for the sedimentary layers

From the processing and inversion of surface wave it is reasonable to affirm that in the Visp area the bedrock is overlain by three main layers (see paragraph 3.2, and in particular Fig. 5). Collating this geophysical structure with available geological information [40], it is possible to identify these layers as, from top to bottom, alluvial, glaciolacustrine and moraine deposits. We attributed to each of these three layers and to the hafspace an average S-wave velocity value $\overline{V_S}$ obtained as a weighted mean of the corresponding V_S from the 10 velocity profiles derived from the inversion of the small-aperture array surface wave data (Fig. 5):

$$\overline{V}_{S_i} = \frac{\sum_{j=1}^{10} H_{i,j} V_{S_{i,j}}}{\sum_{j=1}^{10} H_{i,j}} \quad (1)$$

where the suffix *i* refers to the layer number (*i* = 1, 2, 3, 4), *j* is the index
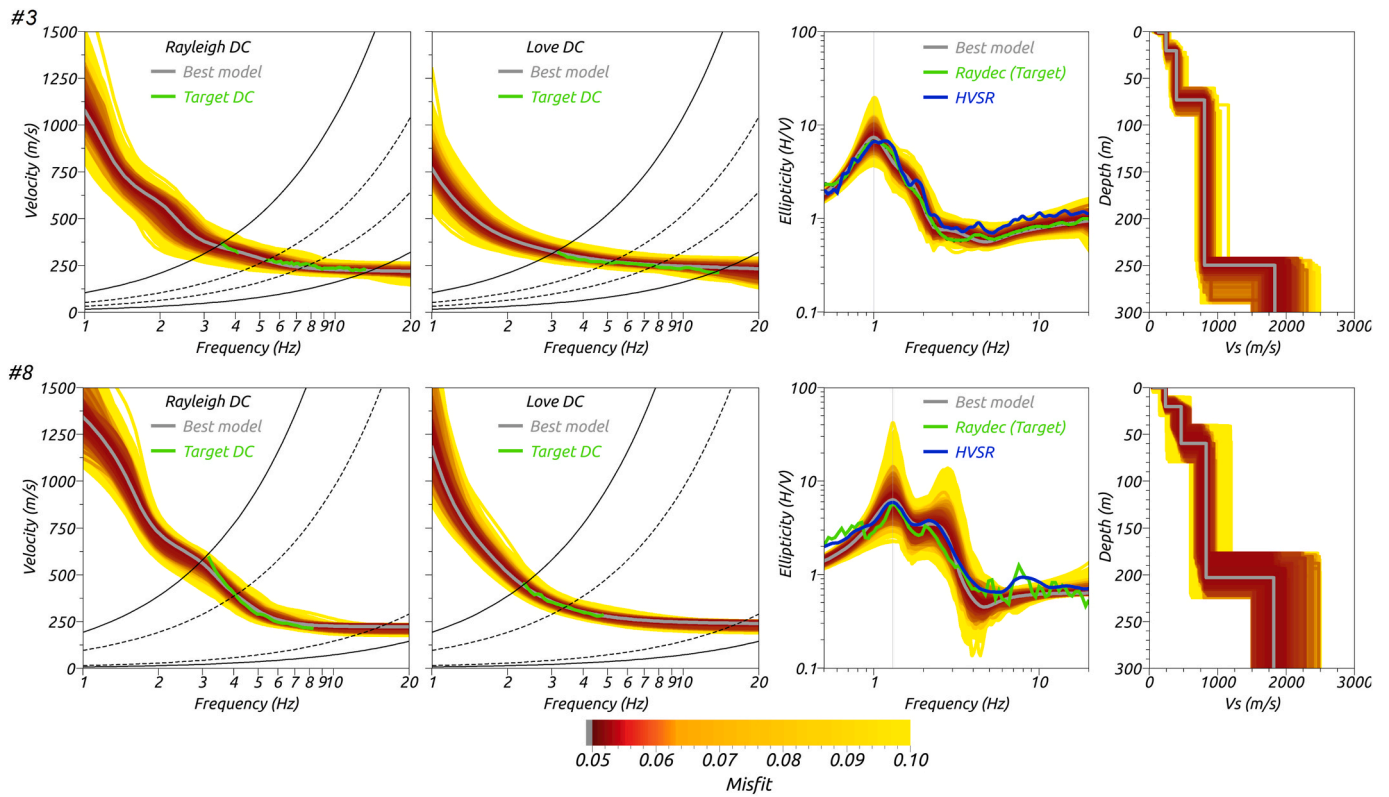
Fig. 4. Example of inversion results for the site #3 and #8 (see location in Fig. 1) considering 5 layers. From left, target and modelled Rayleigh, Love and ellipticity curves. To the right, inverted V_S profiles, with the best one highlighted in grey. Continuous and dashed black lines in the dispersion-curves graphs show the array resolution.
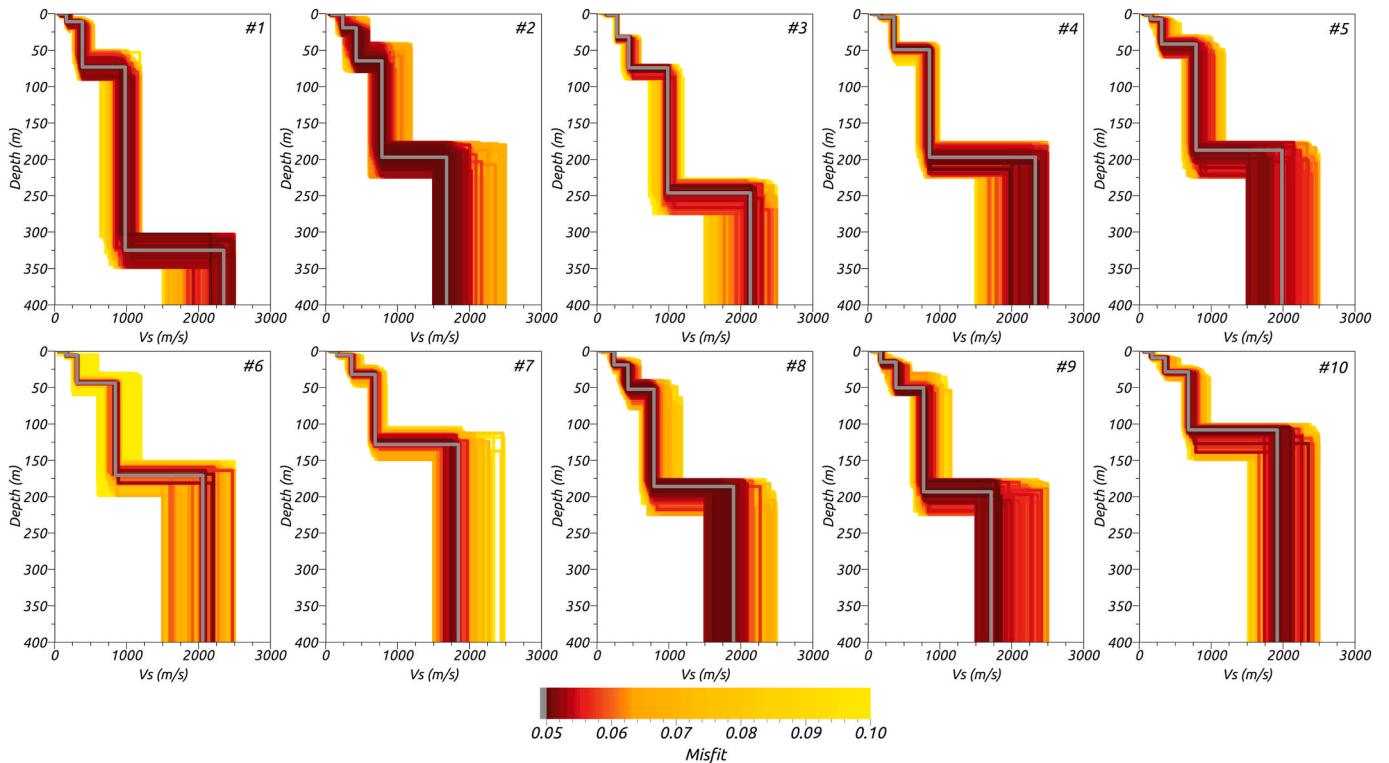

Fig. 5. Best fit V_S profiles (grey lines) for the considered small aperture arrays plotted with generated V_S models (coloured lines with the respective misfit).
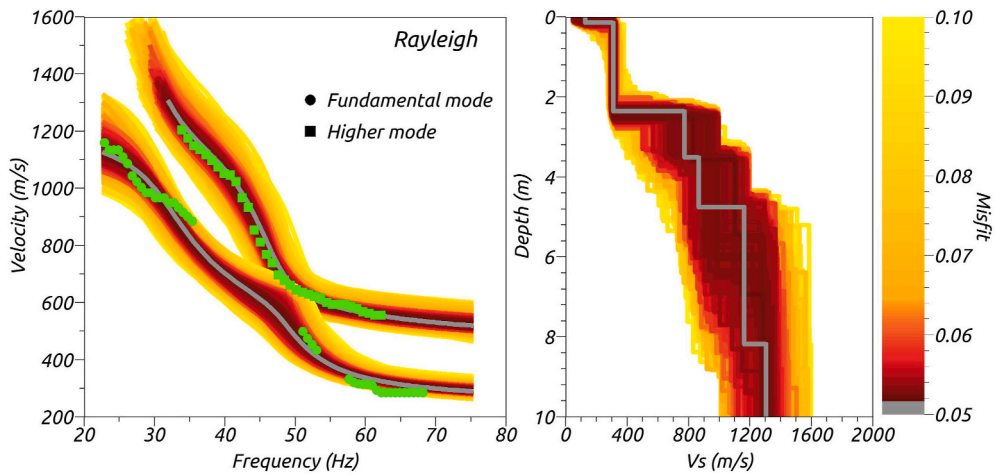
Fig. 6. Dispersion curves and shear wave velocity profile obtained from the inversion of the experimental dispersion curve (green circle fundamental mode and square 1st higher mode) from MASW performed in the rock site in Visp nearby seismic station SVIO (see location in Fig. 1). Left panel V_S profiles produced by the inversion process. The best models for dispersion curves and V_S profile are highlighted in grey.

running through the 10 inverted velocity profiles and H indicates the thickness of the layers of such profiles. The corresponding standard deviation is given by:

$$s\left(V_{S,i}\right) = \sqrt{\frac{\sum_{j=1}^{10} H_{i,j}\left(V_{S\,i,j} - \overline{V}_{S_i}\right)^2}{\sum_{j=1}^{10} H_{i,j}}} \tag{2}$$

The estimated average V_S is 210 ± 53 m/s, 381 ± 44 m/s and 850 ± 103 m/s for the first, second and third layer, respectively. The bedrock is instead characterized by an average V_S of 2030 ± 240 m/s. Note that the third layer (constituted by moraine) is generally more than 100 m thick and the constant-velocity approximation in this case may be too

simplistic, since it doesn't take into account the effect of sediment compaction. The simplest way to represent the effect of the lithostatic pressure, is to introduce a positive velocity gradient varying with depth (e.g. Ref. [56]). Therefore, we retrieved for this third layer a gradient that is equivalent, in terms of travel-time, to the obtained homogeneous velocity value obtained from the inversion. For this purpose, the obtained V_S profiles were used to compute the time average $\Delta T_{Si,j}$ for the j profile and i layer defined as:

$$\Delta T_{Si,j} = \frac{Z_{i,j}}{V_{S\,i,j}} \tag{3}$$
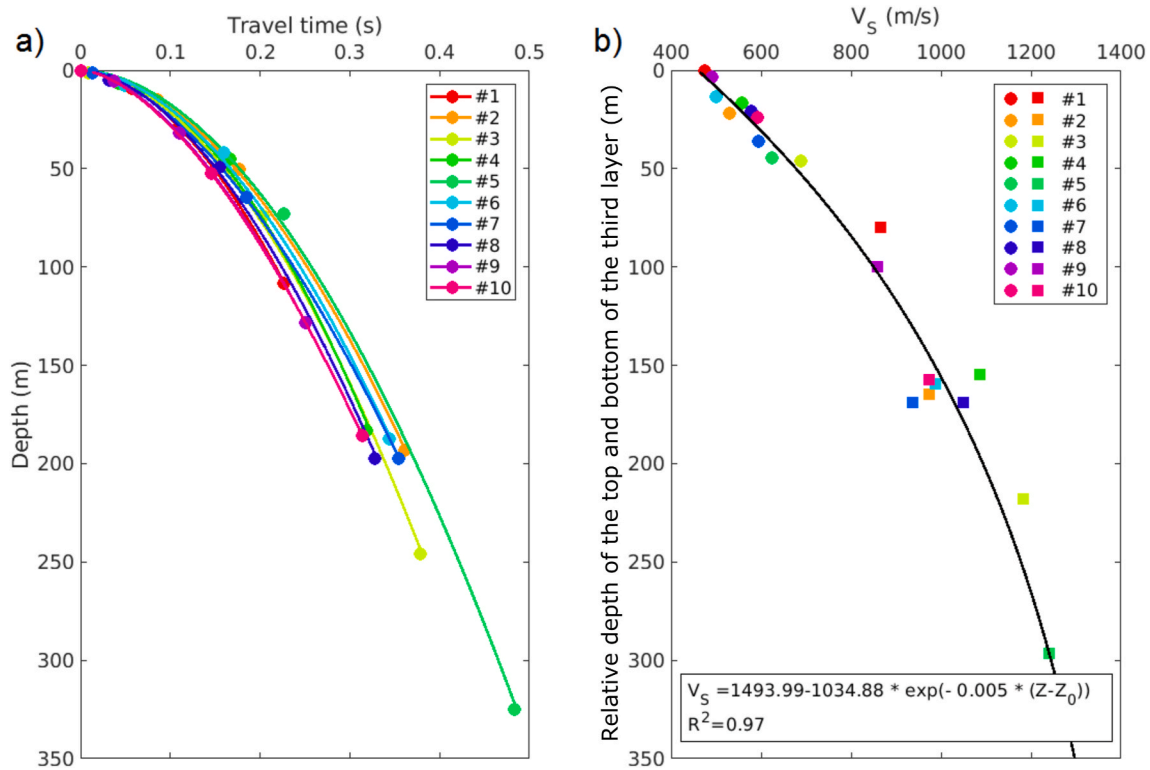

Fig. 7. Left panel travel time vs. depth function for each obtained shear wave profiles (coloured lines). Right panel scatterplot of the top (coloured circles) and bottom depth (coloured squares) V_S estimated at each velocity profiles using the travel time versus depth functions. The black line is the fitted exponential law, which relationship is shown in the graph.

where $Z_{i,j}$ is the depth to the bottom of the layer. The $\Delta T_{Si,j}$ versus depth were then plotted in Fig. 7a and for each profile the travel time function (TT_{Sj}) was calibrated using a power law [57,58]:

$$TT_{Sj} = a_j Z^{b_j} \tag{4}$$

Using the TT_{Sj} functions for each velocity profile the top and the bottom layer V_S values for the third layer were estimated (coloured dots and squares in Fig. 7b). Results show that V_S in the third layer has an initial (average) value of 487 m/s and increases to 1300 m/s after about 300 m. These data were fitted to formulate an exponential law expressing the gradual increase of velocity with depth in the third layer (black line in Fig. 7b):

$$V(z) = V_{Smax} + (V_{Smin} - V_{max})e^{-k(Z-Z_0)} \tag{5}$$

representing the behaviour of V_S in the third layer. In (5) V_{Smin} and V_{Smax} are respectively the minimum and maximum velocity, Z is the depth of interest and Z_0 is the most shallow depth of the top of the layer.

P-wave velocity values inferred from the inversion were not considered reliable as the input data are not sensitive to this parameter [59]. We therefore followed an approach similar to the one just outlined and introduced a travel time (TT_P) function for V_P having the analytical form shown in Eq. (4). Its calibration was based on the interpretation of earthquake time-series recorded at the borehole station SVISP (see location in Fig. 1). This station, active between 2015 and 2019, consisted of 4 accelerometers installed at 0.5, 15, 58 and 102 m depth (Fig. 8a).

We selected 18 earthquake recordings (Table 1, out of a total of 50) characterized by a very good signal-to-noise ratio to reduce the uncertainty on the P-wave arrival time estimation. The picked first breaks on the four accelerometers for each event were then used to build the TT_P function shown in Fig. 8b. We also draw the V_P velocity profile at the station SVISP using the time average and depth interval related to the position of the accelerometers (blue line in Fig. 8c).

We then used the obtained continuous travel-time function TT_P (red line in Fig. 8b) and the estimated depth of the top and bottom of each layer (Fig. 5) to derive the corresponding V_P values for every layer at each of the 10 profiles obtained from the processing of array measurements. We used the following relationship:

$$V_{P\,i,j} = \frac{H_{i,j}}{TT_{P\,i,j,\,bottom} - TT_{P\,i,j,\,top}} \tag{6}$$

where $TT_{P\,i,j,\,bottom}$ and $TT_{P\,i,j,\,top}$ represent the travel time to the bottom and the top of the i-th layer at the j-th profile, respectively (indexes i and j are the same as in eqs. (1) and (2)). The average V_P values and their residuals for the three sedimentary layers were then defined as in Eqs. (1) and (2), leading to 914 ± 176 m/s, 1571 ± 110 m/s and 2355 ± 177 m/s for the first, second and third layer, respectively.

As in the S-wave case, we let the P-wave velocity follow a velocity gradient in the third layer. We therefore define a functional form similar to the one in Eq. (5) to track the V_P/V_S ratio with depth:

$$V_P/V_S(Z) = (V_P/V_S)_{max} + [(V_P/V_S)_{max} - (V_P/V_S)_{min}]e^{-k(Z-Z_0)} \tag{7}$$

where $(V_P/V_S)_{min}$ and $(V_P/V_S)_{max}$ are the minimum and maximum ratio (Z and Z_0 have the same meaning as in Eq. (5)). Note that here V_P is the expected velocity at the top and bottom of the third layer as estimated using the TT_P function (Fig. 8b) and Eq. (6). The V_P/V_S ratios for the third layer at the 10 sites where V_S is estimated from array measurements and V_P from Eq. (6) are as high as 3.54 at the top of the layer (corresponding to $\nu = 0.46$) and decrease to 2.42 (corresponding to $\nu = 0.40$) after about 300 m (Fig. 8d).

The final velocity values for the sediment cover, together with density estimates from available literature [54], are summarized in Table 2.

4.2. Estimation of velocity for the bedrock formation

From the analysis of the MASW results (see section 3.2) it is reasonable to affirm that the intact rock at the surface has a V_S of about 1000 m/s, progressively increasing with depth. In order to obtain an S-wave velocity profile valid for the bedrock at larger depth, we had to adopt a different strategy than the one based on the procedure in Poggi et al. [55]. The method relies on the information coming from the
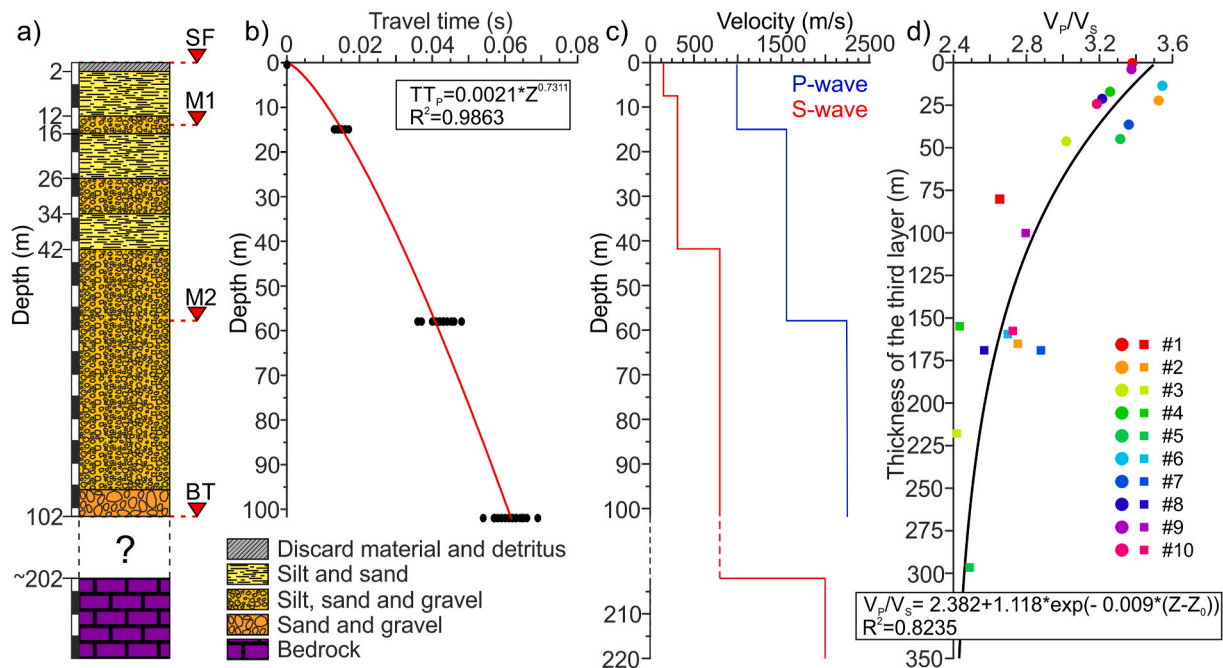

Fig. 8. a) Stratigraphy of the SVISP borehole station with related accelerometer locations at depth; b) Travel time vs. Depth function (red line) in which the black dots are travel time from the considered events; c) Best V_S profiles for the array number 5 (see location in Fig. 1) and P-wave velocity profile obtained for the SVISP station using travel times and accelerometer depths; d) V_P/V_S versus depth function for the third layer (black line) and estimated V_P/V_S values at the top (coloured circles) and at the bottom (coloured squares) of the 10 velocity profiles.

Table 1
Earthquakes used to pick the P-wave arrival time.

ID	yyyy-mm-gg	hh:mm:ss.ms	Dist.	Az.	Lon.	Lat.	Dep.	Ml
1	2015-10-14	00:13:45.06	27.3	97.2	7.525	46.331	4.356	3.10
2	2016-01-02	10:42:44.60	27.1	200.6	7.997	46.529	6.870	3.11
3	2016-03-27	20:02:50.33	6.0	305.6	7.941	46.269	6.642	1.44
4	2016-03-30	19:39:19.94	27.9	247.7	8.212	46.395	5.943	2.12
5	2016-05-04	23:36:19.41	4.9	326.5	7.913	46.264	2.744	0.75
6	2016-10-03	06:43:43.46	63.9	230.1	8.513	46.669	4.940	3.25
7	2016-10-24	14:44:11.58	23.1	100.5	7.580	46.338	8.241	4.14
8	2016-10-24	14:45:04.24	23.3	101.9	7.580	46.343	7.645	2.84
9	2016-10-25	01:42:14.08	23.1	99.2	7.580	46.334	8.152	2.61
10	2016-11-07	23:33:53.70	23	101.3	7.582	46.341	8.063	2.12
11	2017-03-06	20:12:07.40	105	230.1	8.925	46.907	4.223	4.63
12	2017-04-29	00:21:54.85	2.8	107.9	7.843	46.308	6.413	1.00
13	2017-04-29	00:32:27.24	2.8	83.7	7.841	46.298	6.324	0.25
14	2017-04-29	00:44:09.65	2.9	92.4	7.839	46.302	6.718	0.86
15	2018-07-20	22:20:35.49	32.9	3.1	7.861	46.005	6.692	2.60
16	2017-10-08	08:22:31.48	30.6	324.4	8.113	46.076	3.354	1.95
17	2018-10-14	04:25:26.54	4.6	25.3	7.853	46.263	3.760	2.33
18	2018-12-05	02:14:45.58	16.6	110.7	7.674	46.353	5.321	1.57

Table 2
Geophysical properties for the sediment cover for Visp area.

Layer	V_P (m/s)	V_S (m/s)	V_P/V_S	Density (kg/m^3)
First (alluvial deposits)	914	210	~4.4	1795
Second (glaciolacustrine deposits)	1571	381	~4.1	1900
Third (moraine deposits)	–	$1494 - 1035e^{-0.005(Z-Z_0)}$	$2.38 + 1.12 e^{-0.009(Z-Z_0)}$	2000–2200

empirical amplification function (EAF) at station SVIO of the Swiss strong motion network (SSMNet) located on a rock outcrop in Visp (see location in Fig. 1). The EAF referred to Swiss rock model defined in Poggi et al. [55] is computed automatically by the Swiss Seismological Service every time an earthquake is recorded at the station based on an inversion procedure described in Edwards et al. [60]. Poggi et al. [55] compared 27 quarter-wavelength velocity profiles (V_{QWL}) from Swiss seismic stations with the related EAF. In particular, the authors estimated in the log space linear regression between EAF and V_{QWL} in a set of discrete frequencies in the range 1–15 Hz. Using this set of regressions between amplification values and V_{QWL} from the EAF at SVIO a corresponding V_{QWL} profile was determined (Fig. 9b). Therefore, the same global optimization procedure as described in Poggi et al. [55] is used to derive from the derived V_{QWL} at SVIO a simplified gradient reference rock velocity model for Visp. After applying the global optimization procedure to the computed V_{QWL} profile, the outcome profile for Visp (Fig. 9c) is given by the following equation:

$$V_{S_{bedrock}} = (3260 - 1000)\left(1 - 2.7^{\frac{Z_{top}-Z}{207.6}}\right) + 1000 \qquad (8)$$

where 1000 m/s is the minimum V_S as obtained from the MASW analysis, whereas 3260 m/s is the expected maximum velocity at 4000 m depth, according to Husen et al. (2003) P-wave velocity converted into V_S assuming a V_P/V_S ratio of 1.73. This value is within the typical range for sandstone and other well-consolidated rocks [61,62]. The density for the bedrock is taken from Rosselli [54] and set equal to 2700 kg/m^3. In Fig. 9c the derived reference-rock velocity model for Visp is compared with the Swiss one (Fig. 9c). Although the lithology of the bedrock in the Rhone valley is variegated and changes from granite to gneiss in the North part to limestone in the South part depending on the position along the valley, we assume homogenous physical properties within the
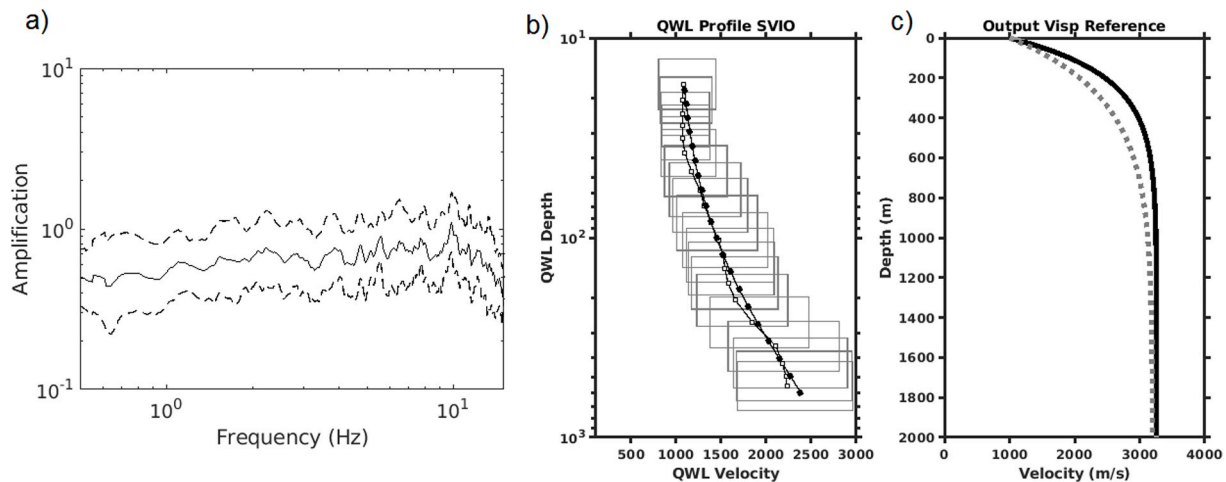

Fig. 9. a) Empirical amplification function mean (black line) and standard deviation (dashed black lines) at SVIO site obtained through empirical spectral modelling [60] and referred to the Poggi et al. [55] Swiss reference rock velocity profile. b) V_{QWL} profile (white squares) obtained using correlation functions between V_{QWL} and amplification factors from spectral modelling of earthquake spectra as in Poggi et al. [55] for the SVIO site and its related uncertainties (grey squares). Black dots represent the inverted V_{QWL} profile. c) Best velocity profile in gradient form achieved from global optimization procedure (black line) and Swiss reference rock model (grey dotted line).

area under study for the bedrock.

4.3. Geometry of the basin

In a first step, we defined the borders of the valley bed, intended as the transition between soft sediments and surrounding competent rock units, based on the geologic map (Fig .1) and the precise digital elevation model describing the surface of Switzerland without vegetation and constructions (grid 2 × 2 m) available for the area swissALTI3D (Swisstopo, 2020). The obtained results can be considered acceptable, even though the bedrock is covered by shattered rock deposits in some areas along the northern and south-eastern borders (see Fig. 1).

The sedimentary cover thickness (H), coming from both the inversion of geophysical data (V_S profiles, gravimetric measurements) and direct borehole observations, were plotted versus f_0 from HSVR in a scatterplot (Fig. 10), displaying a non-linear trend with frequency.

Taking into account that f_0 far from the basin edge is quite well correlated with bedrock depth, whereas close to the basin edge the correlation is hindered by edge effects [63,64], we applied a power law as proposed by Ibs-Von Seth and Wohlenberg [24]:

$$H = a*f_0^b \qquad (9)$$

where a and b are the regression coefficients. In particular, to take into account the difficulties related to the edge effects we performed and compared two fits. The first fit (Fit 1 in Fig. 10) was performed using H coming from Rosselli and Olivier [37] gravimetric data inversion and picked f_0 (Fig. 10). The gravimetric depth seems to be generally well correlated with f_0, except towards the borders. The second regression (Fit 2 in Fig. 10) was based on H from boreholes (see location in Fig. 1) and from the results of the joint inversion with the corresponding f_0. These two data fits are in good agreement but they diverge somewhat at high frequency and for thinner layers. We then consider the second fit as the more reliable one, because it is constrained in the f_0 frequency range 1.5–9.0 Hz with borehole data and inverted velocity profiles.

The thickness of the sedimentary cover was then estimated converting f_0 at each HVSR point using Eq. (9) and a contour map with a resolution of 10 m was produced based on kriging interpolation (third layer map in Fig. 11) motivated by the heterogeneous data distribution (see Fig. 1). We used the VESPER (Variogram Estimation and Spatial Prediction with ERror) software [65] developed by the Australian Center for Precision Agriculture (ACPA) since it is capable to perform
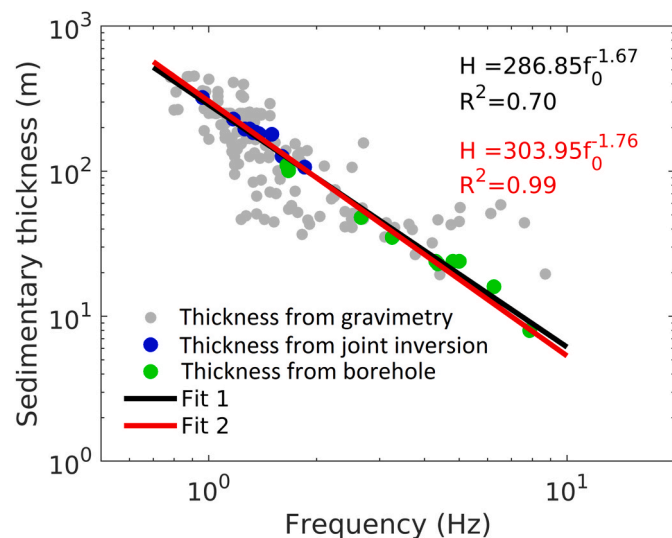
kriging with local variograms [66]. Briefly, kriging with local variograms allows: i) to search for the closest neighbourhood for each prediction site, ii) to estimate the variogram from the neighbourhood, iii) to fit a variogram model to the data and iv) to predict the value and its uncertainty. We tested the spherical and exponential variogram, preferring the former because it results in a smaller root-mean-square residual. The obtained values were then smoothed to reduce the presence of spikes associated to isolated data points by using a non-linear filter having size 15 × 15 pixels.

As described in section 4.1, three main layers were found for the sedimentary basin based on array measurements and surface wave data inversion. Contour maps of the depth to each interface were obtained using a similar kriging procedure as the one described for the bedrock. In particular, the first (shallowest) discontinuity (Fig. 11) was constrained using 74 boreholes (Fig. 1) and the inverted V_S profiles (Fig. 5). The corresponding layer has a thickness varying between 1 and 11 m, with higher values occurring along the Rhone river, and it can be related to the upper alluvial deposits mainly composed by silt and sand.

The second discontinuity map (Fig. 11), between the second and the third layer, was instead more difficult to obtain due to the low number of direct information coming from deep boreholes. For this reason, the depth to second interface was determined by inverting single station ellipticity curves extracted from 100 of the 200 ambient vibration measurements used in this study (Fig. 12). The geophysical model in Table 2 assuming a homogenous bedrock, having the V_S obtained by Eq. (6) at the bedrock depth, was used for the parametrization together with the depth to the first and last (i.e. bedrock) interface previously constrained. For each site 200,000 models were generated, allowing to the input velocity profiles to vary up to 20% of their original value. Therefore, the depth of the second interface coming from the best inversion result was used to derive the geometry of the second discontinuity.

5. 3D model validation

5.1. Testing 1D velocity profiles comparison with gravimetric and geological data

The final 3D velocity model (Fig. S2 of the supplementary material) was validated by extracting 1D velocity profiles at selected locations (marked by letters in Fig. 1) and comparing the relative measured and theoretical ellipticity curves. Although this alpine valley is probably characterized by 2D/3D effects, but not 2D/3D resonances, the 1D assumption can be considered valid for sites far from the borders [64]. The two sets of curves, shown by black and green-dashed lines in Fig. 12, are generally in good agreement. The observed discrepancies in term of frequency of the fundamental peaks are probably due to the uncertainties in discontinuities depth and layer velocities linked to the kriging method used to interpolate the subsoil model.

A further comparison was made between the bedrock map as obtained in this study and the gravimetric model of the Rhone valley [37]. Although the gravimetric model is not a high-resolution model, the comparison evidences a similar bedrock shape and good correspondence in terms of depth to bedrock values (Fig. 13).

The main differences are observed along the edges as shown by the cross-sections in Fig. 13. These discrepancies can be explained considering the particular attention paid in this study to define the valley edges (rock to sediment contact) and considering that the gravimetric model was derived using a limited number of transects along the Rhone valley [37]. The scale of features which can be identified with a gravimetric survey depend on the grid spacing used for the survey compared with the size and shape of the investigated feature [67].

Finally, we compared the 3D geological model of Visp obtained in the frame of the GeoQuat project [40] with this study model. The results highlighted that 80% of the lithology contained in the first layer of the 3D geophysical model are upper deposits (mainly silt linked to flooding
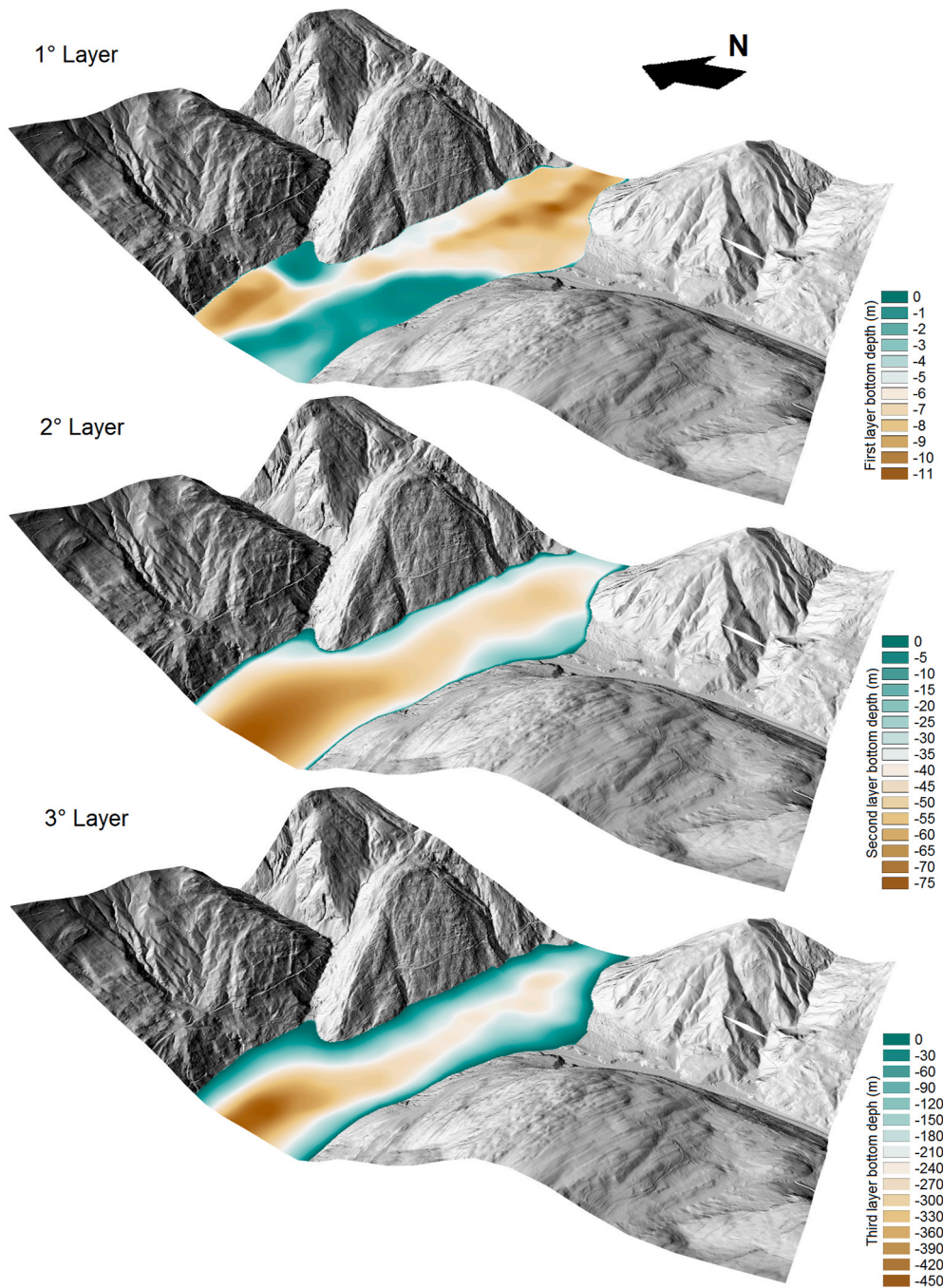
Fig. 10. f_0 vs. H scatter plots, with the corresponding regression curves Fit 1 (f_0 vs. H from gravimetric technique) and Fit 2 (f_0 vs. H from borehole and geophysical data).

Fig. 11. Contour maps of the first, second and third layer bottom depth from the surface of the 3D geophysical model, obtained by using spherical local variogram method with kriging algorithm. The contour maps are plotted on the relief map with the permission of Swisstopo JA100120.

episodes). From the comparison, the second layer of the 3D geophysical model is composed for 90% by lower deposits (gravel and sand carried inside the river bed). The GeoQuat model does not resolve the bedrock, because it relies mostly on borehole profiles of limited depth (<30 m).

5.2. Modelling 3D ambient vibrations

To further validate the velocity model, we compared synthetic and measured HVSR spectral ratios at several locations in the sedimentary basin. We did not consider only peak values, but verified whether the whole curve was well reproduced.

Three-dimensional ambient noise simulations for the Visp velocity model were carried out by using SW4 code [68,69], a fourth-order finite-differences numerical package that solves the equation of motion in displacement formulation. The input model measures 6100 m along the x axis (easting), 7800 m along the y axis (northing) and 4000 m along the z-axis (depth). The model was discretized with a grid step of 40 m and a mesh refinement at $z_1 = 1000$, $z_2 = 700$, and $z_3 = 480$ m, resulting in at least 12 grid points per wavelength at 4.0 Hz. In fact, the refinement command in SW4 enables to locally refine the computational mesh in areas where finer resolution is needed [68,69]. As a result, the composite grid contains mainly four level grids, where the coarsest has a grid size of 40 m and it covers the bottom of the model ($z_1 \leq z \leq 4000$ m). The next refined grid has half grid size (20 m) and covers the depth range $z_1 \leq z \leq z_2$, whereas the grid size in the third level is refined by another factor 2 (10 m) and it spans $z_2 \leq z \leq z_3$. Finally, z_3 indicates the
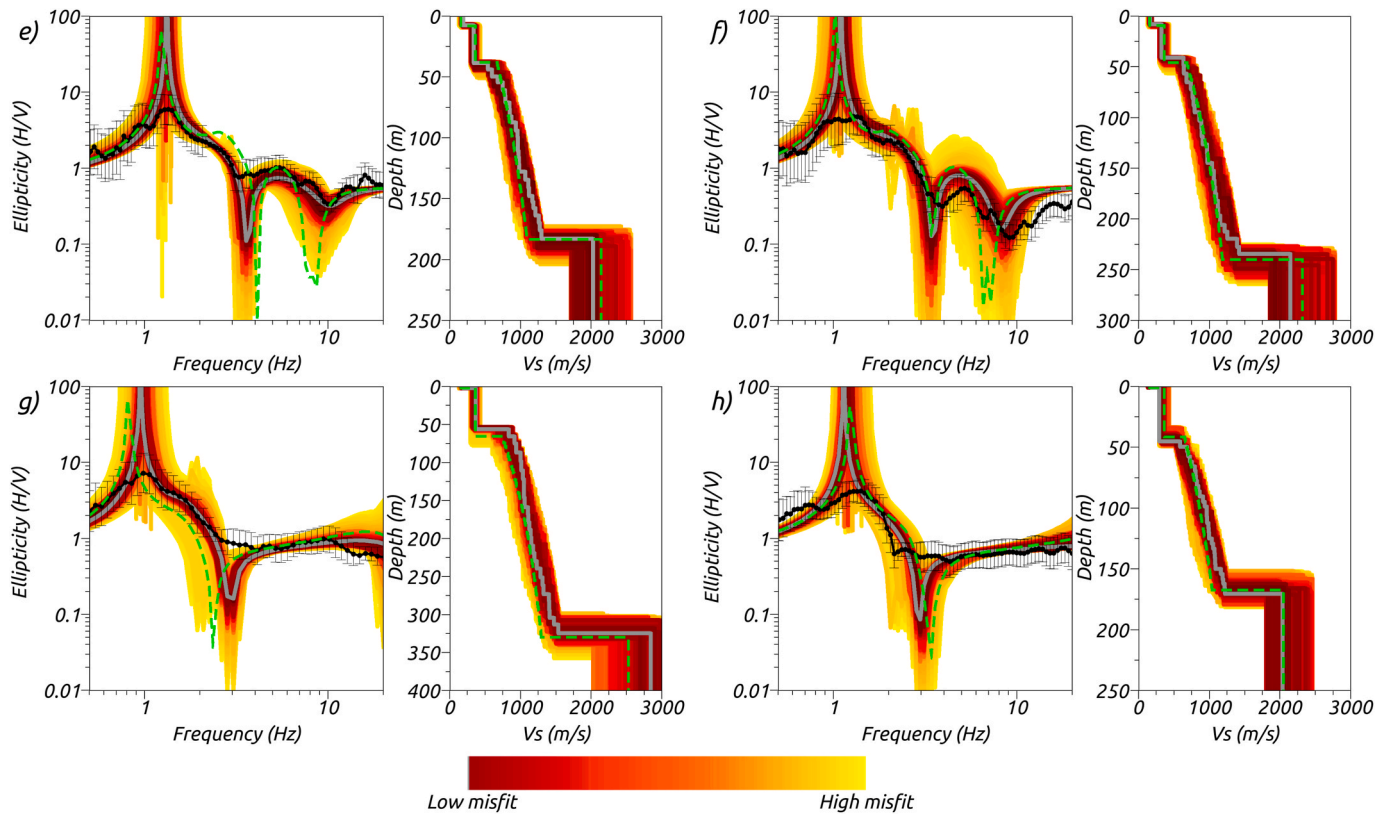
Fig. 12. Examples of ellipticity inversion for selected sites (the sites with the corresponding letters are shown in Fig. 1). The black lines and corresponding bars are the measured ellipticity and its standard deviation; The grey lines instead show the best fitting ellipticities and corresponding velocity models obtained from the inversion process; The coloured lines are the generated models during inversion as a function of misfit; The green dashed lines are instead the velocity models extracted for the sites from the 3D model, with the corresponding ellipticity curve.
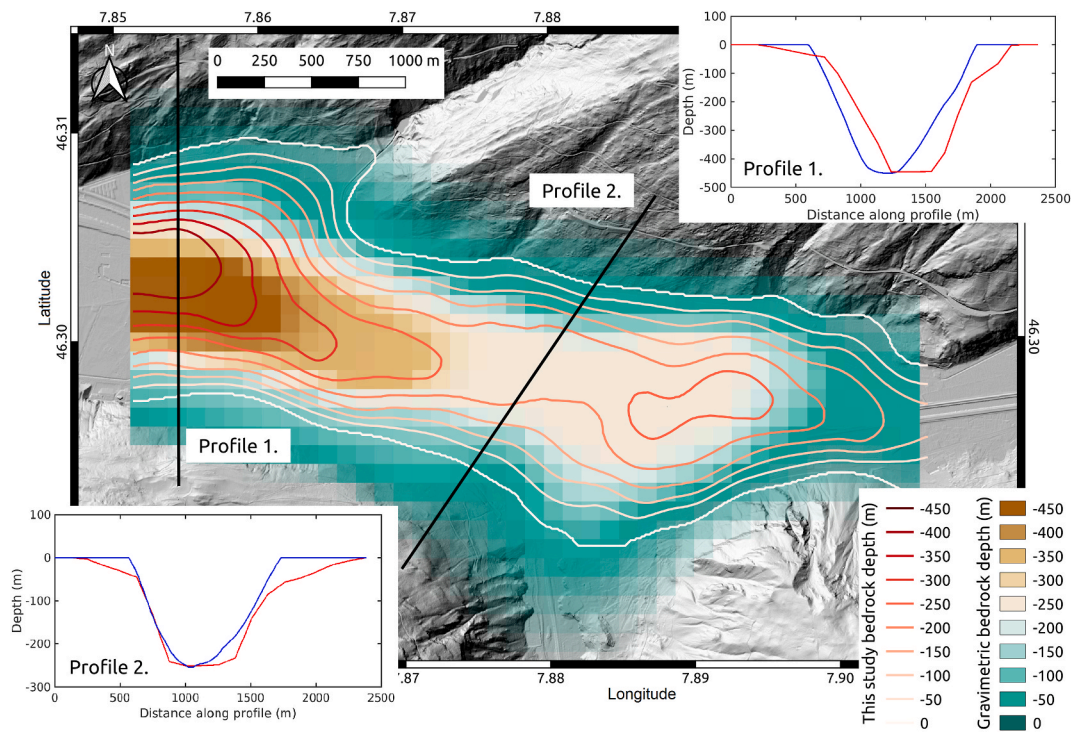

Fig. 13. Bedrock depth obtained through gravimetric measurements [37]. For comparison, the bedrock depth isolines obtained in our study is given. The upper right and lower left panels show the profile across the valley where blue lines are referred to this study model and the red ones to the gravimetric model. The contour maps are plotted on the relief map with the permission of Swisstopo JA100120.

starting depth of the grid size 5 m which covers the model up to the top surface. The total number of grid points with this configuration is 2.030 × 10⁸. The SW4 code works with a free surface condition on the top boundary and absorbing super-grid conditions on the far-field boundary [70]. The super-grid damping layer at the sides and bottom of the model prevented spurious reflections from contaminating the computed ground motions. Intrinsic attenuation and topography were neglected after a few tests, since we found that they did not influence sensibly the synthetic spectral ratios. In particular, topography was not considered since we did not model the site response of the rock outcropping on the basin edges; the simulation results cover only the valley floor hosting unconsolidated sediments. To reproduce the diffusive nature of ambient vibrations, we deployed 5000 impulsive single-forces randomly located in the sedimentary basin, with amplitudes in the 0 to 1 range. Sources orientation was normally distributed around the vertical, in order to excite a consistent amount of Rayleigh waves. Our simulations were 135 s long, although the first 15 s were discarded because of non-stationary wavefield amplitude (see example in Fig. S3 of the supplementary material). We compensated the relatively short duration of the synthetic time-series (dictated by their computational cost) by considering three sets of simulations, each characterized by a different seed number for the generation of the random source parameters.

We produced three sets of ground motion simulations at 22 seismic station sites evenly distributed in the basin (Fig. 14), where each set was characterized by different source properties determined by different seed numbers. Although microtremor velocity spectra are normally used

to compute HVSR, displacement or acceleration spectra can be used as well [71]. The displacement time-series were then processed with Geopsy following a workflow very similar to that applied to the field data. We chose a window length of 40 s with a window-overlap of 50%. The window length was chosen such that the resolution at lower frequencies is well guaranteed in the spectral ratios. A Konno and Ohmachi [47] smoothing b = 40 was applied to the spectra. A comparison between experimental and modelled HVSR spectral ratios at four representative locations is shown in Fig. 14 (in the Supplementary Material Figs. S4 and S5 are reported the results related to the other 18 sites).

We found an overall good agreement between synthetic and observed spectral ratios, particularly in terms of fundamental frequency, likely indicating realistic depth to bedrock values and fairly accurate physical properties. Although the whole curve was in general well reproduced at most stations, we noticed that our velocity model often predicted lower ratios than otherwise observed. Following Bonnefoy-Claudet et al. [22]; we speculate that this systematic difference is mainly associated to the relative amount of Rayleigh and Love waves in the simulated wave field, which may not reflect real conditions. Second order differences in the spectral ratios could be related to the bedrock in the Rhone valley that is variegated and changes from granite to gneiss in the North to limestone in the South depending on the position along the valley. This aspect is well highlighted if we subdivide the points where synthetic HVSR amplitude is higher or lower with respect the experimental one at the fundamental frequency (Fig. 14). Although, we tried to adjust the model in some points accordingly with the comparison
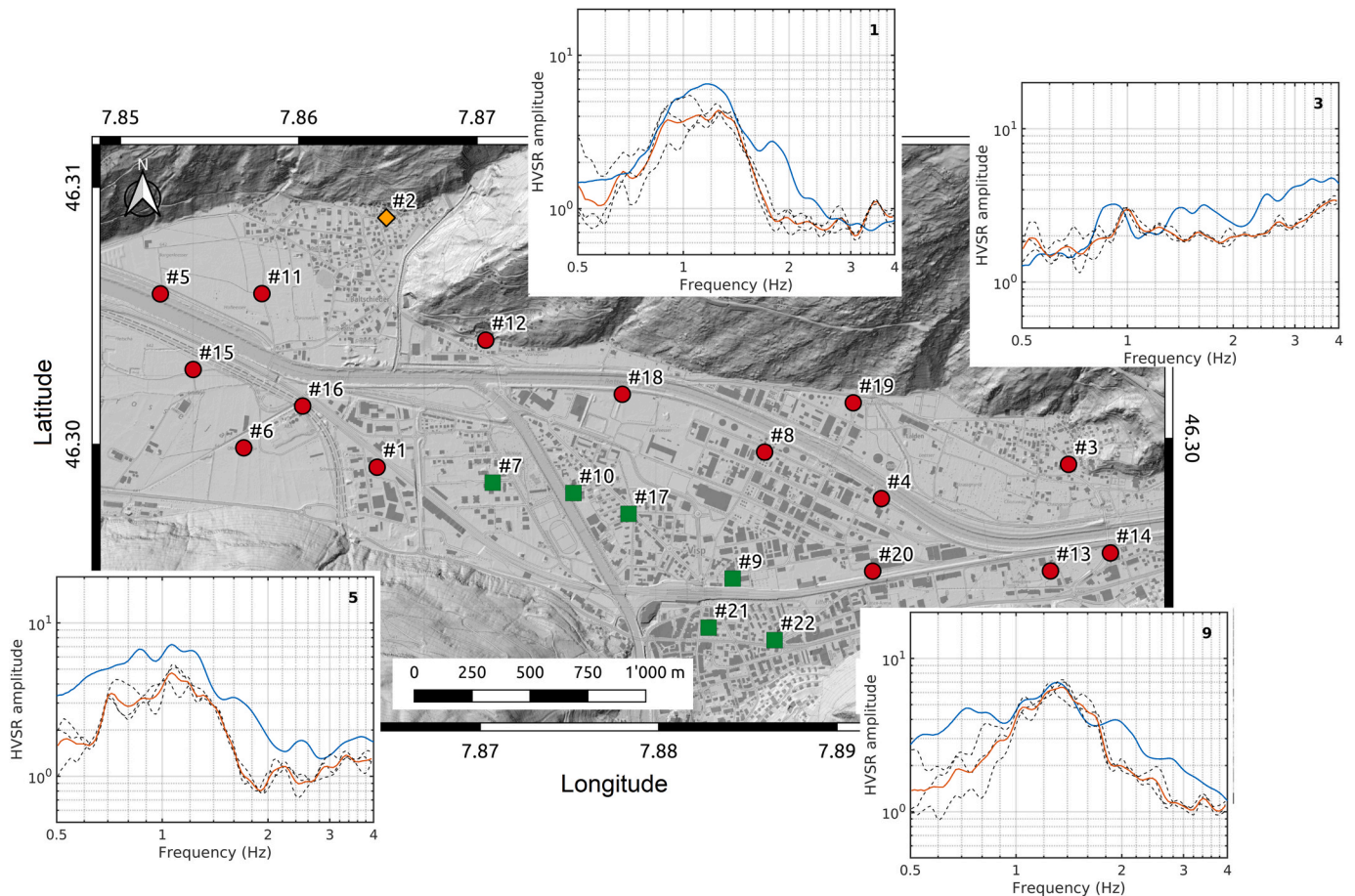

Fig. 14. Example of synthetic (dashed black line) and observed (blue line) HVSR spectral ratios at four representative locations in the Visp area. The geometric average of the three individual synthetic ratios is represented in red. In the map green rectangles are sites where the synthetic HVSR is almost equal in amplitude with the experimental HVSR at f₀, whereas red circles indicate places where synthetic HVSR is lower in amplitude with respect the experimental HVSR at f₀. The orange rhombus shows the location of a synthetic that does not match the experimental HVSR. All the comparison between synthetic and observed HVSR are in Figs. S4 and S5 in the supplementary material. The maps are plotted with the permission of Swisstopo JA100120.

between synthetic and experimental HVSR modifying the layer thicknesses, the point #2 (orange rhombus in Fig. 14) is the only one where there is not good agreement between observation and modelling. This site reflects the complexity of the area where the site is located. In particular, it lies on a conoid deposits, which we didn't include in our model.

6. Modelling the earthquake amplification

The validated velocity model was then used to obtain seismic site amplification in the area of Visp using Standard Spectral Ratio technique (SSR). The SSR consists in the ratio between the horizontal components of motion at the soft sediment site with respect a reference site on rock
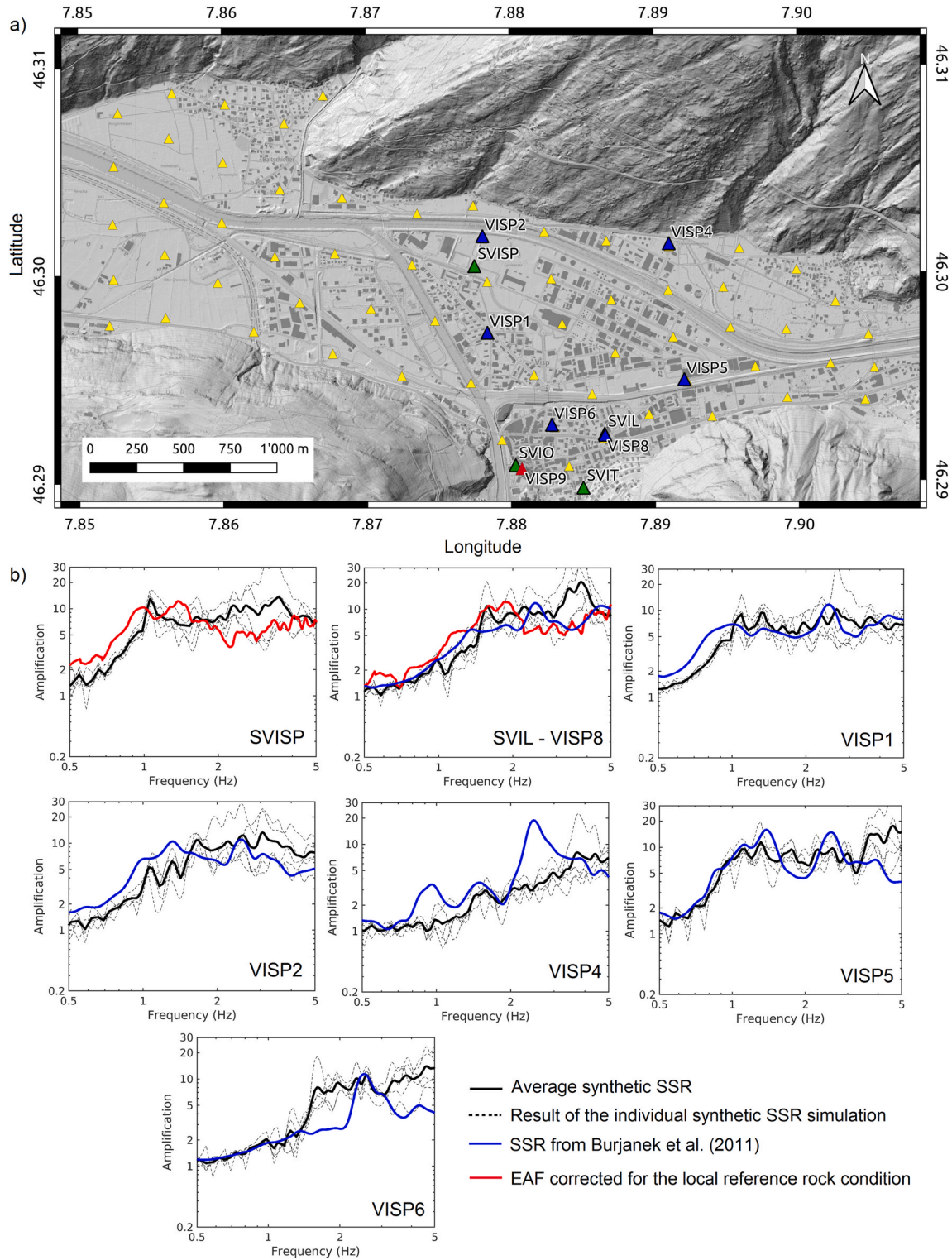

Fig. 15. a) Map showing the location of surface receivers (yellow) chosen to extract synthetic SSR, blue triangles are temporary stations for which Burjanek et al. [73] computed SSR with respect station VISP9 (red triangle) and green triangles are seismic stations of the SSMNet. The maps are plotted with the permission of Swisstopo JA100120. b) Example of synthetic and observed amplification functions at seven locations in the Visp area.

[72]. For our synthetic SSR, we choose 64 surface receivers randomly distributed inside the valley (Fig. 15a). Six of these receiver points correspond to temporary seismic stations instrumented with Quanterra Q330 digitizer and LE3D-5s short period sensor (Fig. 15a). This temporary network collected local and regional earthquakes with local magnitude in the range 0.9–4.0 between 2008 and 2009 [73]. evaluated the seismic site response at these sites through SSR method with respect a local reference site, named VISP9 and positioned only 75 m far from the permanent station SVIO. In the area are also present others SSMNet stations named SVISP, SVIT and SVIL (Fig. 15a) for which EAF are also routinely computed.

To compute the synthetic SSR at the surface receivers we did not use a single reference station on rock outcrop having the characteristics described in Ref. [74]; but we ran simulations twice: the first time considering a parallelepiped-shaped model that does not contain the sedimentary basin and it has the properties of the bedrock shown in Fig. 9, and the second time using the 3D full velocity model of Visp (inclusive of sedimentary basin). In both simulations the sources were placed at the same location. Therefore, the Fourier spectra of the recorded time series at the chosen locations of the full sedimentary basin (soft soil) were divided for the corresponding Fourier spectra of the model without Basin (rock condition). This approach should ensure, that the differences in the travel path can be neglected. For the simulation we used again the SW4 code [68,69] and the same model size employed for the noise simulation. The SW4 code does not allow to simulate the propagation of plane incidence waves and a single source located inside the model is not ideal to generate synthetic SSR since the spectral ratio will strongly depend on the respective radiation pattern (e.g. Ref. [75]. In order to avoid this issue, the 3D model maximum depth was extended to 7000 m and we placed on a horizontal plane at 5000 m depth 5500 point sources randomly distributed with a minimum distance between each other of 300 m. This plane has a length of 3000 m in x-direction and 5000 m in y-direction so that it is sufficiently away from the 3D model borders. This approach can be assumed as being virtually equivalent to a composite source model in which an earthquake is made up of numerous point source sub-events distributed along a plane (e.g. Ref. [76]). All these sources follow a Brune model as source time functions and they trigger at 0 s with the synthetic waveform having a duration of 20 s (see example in Fig. S3 of the supplementary material). The corner frequency of the Brune-functions is chosen to be 1 Hz; strike, dip, and rake of each source are randomly assigned to reproduce the complex source process and to avoid synthetics having at times one component with amplitude much lower than the other (i.e. nearly nodal motions) as highlighted by Zeng et al. [77]. Finally, the moment amplitude is chosen to be 1 and no attenuation is considered in the simulations. We then performed 5 simulations with different sub-events positions and source parameters (strike, dip and rake). This number of simulations was chosen as a trade-off between computational costs and robustness of the results. The final SSR curves at each receiver are the arithmetic averages of the curves obtained by the five simulations with different seed states of the random parameters. The achieved signals were then processed applying the same filter and smoothing as for HVSR. A comparison between synthetic and experimental amplification functions (SSR and EAF) was made to test the reliability of the results (Fig. 15b). This synthetic and empirical SSR dataset are referred to the local reference rock condition (Fig. 9), whereas the EAF are referred to the Swiss reference rock condition [55]. According to Fig. 9 the local reference condition shows a slightly higher V_S entailing an EAF of the SVIO station with amplification level lower than 1 in a broad frequency range.

Considering the proximity and geological homogeneity between VISP9 and SVIO, we assume their site responses to be virtually equivalent, hence the EAF at VISP9 (not measured) can be reasonably approximated by the EAF at SVIO. Therefore, the EAF at SVISP and SVIL (same place of VISP8) were divided with the EAF at SVIO so that the resulting amplification functions are all referred to the local reference site (red lines in Fig. 15b) and can be equated with SSR (blue lines in

Fig. 15b). In fact, the EAF at SVIO represents the ratio between the amplification expected at the local rock site in Visp and the Swiss reference rock model. The comparison between synthetic and experimental amplification functions shows an overall good agreement in all the sites located inside the valley (SVISP, SVIL- VISP8, VISP1, VISP2 and VISP5). The agreement diminishes in the sites located nearby the borders (VISP4 and VISP6) probably because our model near the borders is not too accurate or the lithologic sequence especially for the site VISP6 is more complex.

The amplification values extracted at the different locations were then interpolated using a similar kriging procedure as the one described for the 3D model. This allows us to obtain amplification maps at several frequencies (Fig. 16). As expected, the sediment thickness play an important role on the amplification values. In particular, it is possible to observe that at frequencies lower than 1.0 Hz the main amplification occurs in the West edge of the considered basin portion with values reaching factor 8 in amplification. Instead, at 1.0 Hz the amplification increases up to factors of 15 in the central part of the considered model, where the thickness of the sedimentary cover (200–300 m) causes a fundamental frequency near to 1.0 Hz. Finally, the map at 3.3 Hz clearly shows the role played by the layers 1 and 2 of our model, with the main amplification observed along the river deposits. Such high amplification values are frequently observed at the floor of deeply-incised valleys of the Swiss alpine region, as witnessed by several authors [6,21,46,60].

7. Conclusions

We characterized the main geophysical discontinuities and their properties in the alpine basin in the Visp area based on ambient vibration data and earthquake recordings integrated with borehole information.

The ambient vibrations recorded with small aperture seismic arrays were processed by means of the *f-k* technique to retrieve dispersion curves and to determine 1D V_S profile at several locations, whereas HVSR were used to determine f_0 related to the sediment thickness. The V_S profiles allowed us to highlight the presence of three main layers for which we derived V_S values. The two shallowest layers were considered homogenous and with constant velocity, whereas for the thick third layer the effect of sediment compaction was taken into account by introducing an exponential functional form. The V_P values were determined based on earthquake P-wave arrival times recorded at the SVISP vertical array. For V_S at the bedrock we adopted an approach similar to that proposed by Poggi et al. [55] by extracting from the empirical amplification function for station SVIO a V_{QWL} profile subsequently inverted using a global optimization process.

A relationship between sediment thickness and f_0 was determined following Ibs-Von Seth and Wohlenberg [24]; whereas borehole data were used to infer the geometry of the first layer. The second discontinuity was instead determined by inverting single station ellipticity curves complemented by a scarce number of boreholes measurements reaching larger depths.

The obtained velocity model and the geometry of the bedrock were validated by comparing theoretical ellipticity from extracted 1D profiles with the measured one. Moreover, the gravimetric model of Roselli and Olivier [37] was used for comparison. A comparison of the two surficial layers proposed in a model developed during the GeoQuat project [40] allows us to affirm that there is a good agreement with Rhone and glaciolacustrine deposits. Synthetic HVSR were computed based on three-dimensional ambient noise simulations. The good correspondence between simulated and empirical HVSR further corroborated the accuracy of our model.

Finally, we computed synthetic spectral ratios at specific receiver locations simulating ground shaking, using an approach virtually equivalent to that of a composite source model. The modelled amplification functions were compared with amplification functions obtained by using actual earthquake recordings at temporary and permanent
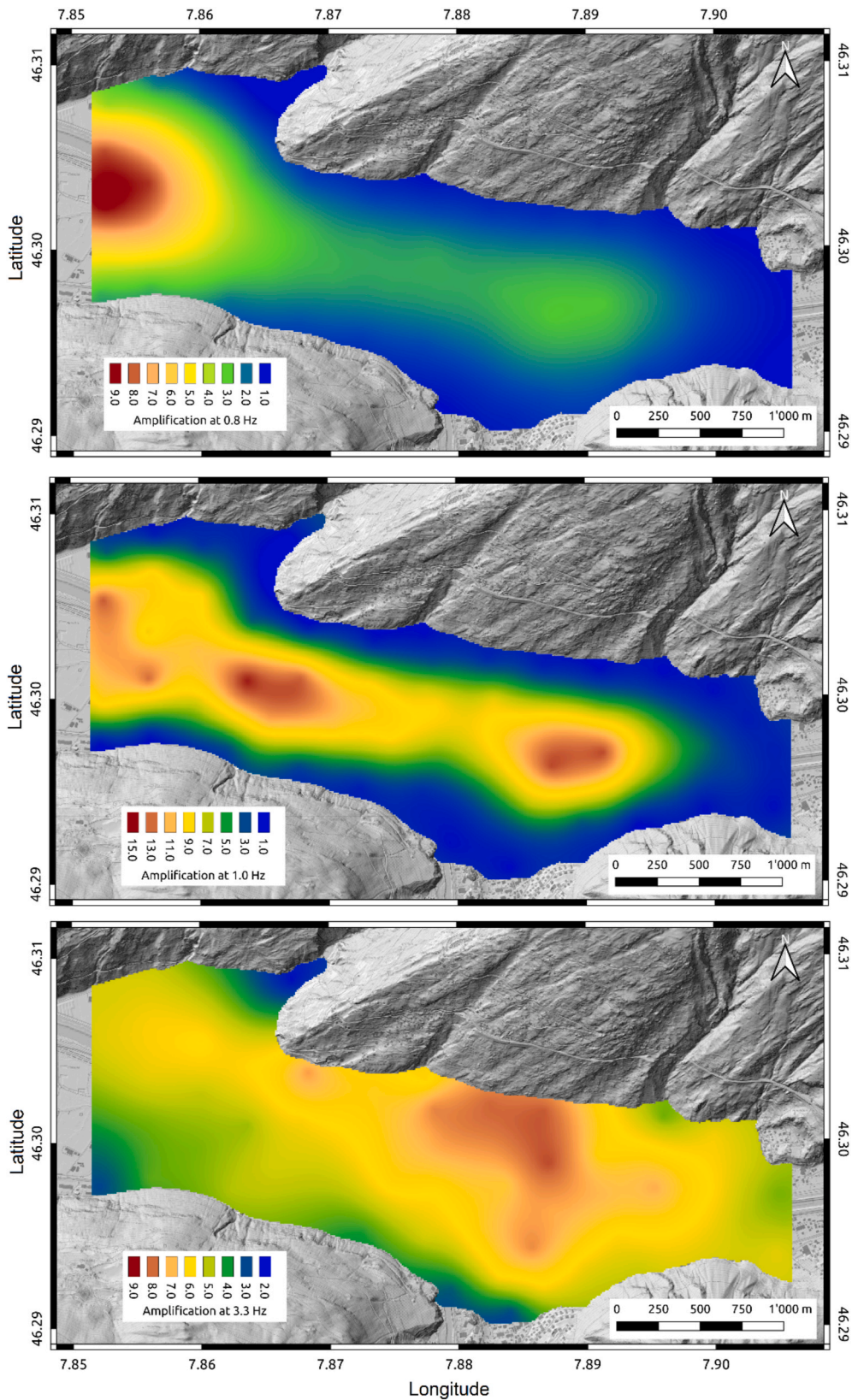
Fig. 16. From top to bottom amplification maps at 0.8, 1.0 and 3.3 Hz obtained from the interpolation using kriging. The amplification values are referred to the local reference rock condition in Visp (see Fig. 9). The maps are plotted with the permission of Swisstopo JA100120.

strong motion stations. The good agreement we obtain confirms the validity of our approach. Finally, kriging interpolation was used to derive amplification maps for different frequencies. The sediment thickness appears to play an important role on the resulting amplification, which reaches factors of 8–15. Such high amplification values are not unusual for valleys of the Swiss alpine region.

This final result suggest that ambient vibration techniques are a powerful and cost-effective tool to reconstruct three-dimensional models of the subsurface that can be used for geothermal, geological, hydrogeological and seismic site response studies.

Consent to participate

Informed consent was obtained from all individual participants included in this study.

Consent for publication

We declare that we have the permission to publish the research findings included in this manuscript.

Funding

Availability of data and material

The data of the Swiss network can be accessed following instruction in the webpage http://www.seismo.ethz.ch/en/research-and-teaching/products-software/waveform-data/(last accessed July 15, 2020). The data of the station site characterization can be access on http://stations.seismo.ethz.ch (last accessed August 20, 2020). The maps and the aerial imagery are reproduced with the permission of swisstopo (JA100120).

Code availability

The SW4 code for the simulation can be accessed in the webpage https://geodynamics.org/cig/software/sw4/(last accessed July 15, 2020) and the Geopsy software used for ambient vibrations processing can be downloaded from the website https://www.geopsy.org/(last accessed August 05, 2018). The maps were produced using QGIS (https://www.qgis.org/last accessed January 15, 2020) and the figures using Matlab. The 3D model pictures in the supplementary material were produced using Paraview https://www.paraview.org/last access November 29, 2021).

Authorship contributions

Conception and design of study: Francesco Panzera, Walter Imperatori, Donat Fäh; Acquisition of data: Francesco Panzera; Analysis and interpretation of data: Francesco Panzera, Jonas Alber, Walter Imperatori, Paolo Bergamo; Drafting the manuscript: Francesco Panzera, Jonas Alber, Walter Imperatopri, Paolo Bergamo; Revising the manuscript critically for important intellectual content: Donat Fäh. All authors approve the version of the manuscript to be published: Francesco Panzera, Jonas Alber, Walter Imperatori, Paolo Bergamo, Donat Fäh.

Declaration of competing interest

The authors declare that they have no known competing financial interests or personal relationships that could have appeared to influence the work reported in this paper.

Acknowledgements

Appendix A. Supplementary data

Supplementary data to this article can be found online at https://doi.org/10.1016/j.soildyn.2022.107163.

References

[1] Wiemer S, Giardini D, Fäh D, Deichmann N, Sellami S. Probabilistic seismic hazard assessment of Switzerland: best estimates and uncertainties. J Seismol 2009;13: 449–78.

[2] Fäh D, Giardini D, Bay F, Bernardi F, Braunmiller J, Deichmann N, Furrer M, Gantner L, Gisler M, Isenegger D, Jimenez MJ, Kastli P, Koglin R, Masciadri V, Rutz M, Scheidegger C, Schibler R, Schorlemmer D, Schwarz-Zanetti G, Steimen S, Sellami S, Wiemer S, Wossner J. Earthquake catalogue of Switzerland (ECOS) and the related macroseismic database. Eclogae Geol Helv 2003;96:219–36.

[3] Fritsche S, Fäh D, Schwarz-Zanetti G. Historical intensity VIII earthquakes along the Rhone valley (Valais, Switzerland): primary and secondary effects. Swiss J Geosci 2012;105(1):1–18. https://doi.org/10.1007/s00015-012-0095-3.

[4] Frischknecht C, Wagner JJ. Seismic soil effect in an embanked deep alpine valley: a numerical investigation of two-dimensional resonance. Bull Seismol Soc Am 2004; 94(1):171–86.

[5] Roten D, Fäh D. A combined inversion of Rayleigh wave dispersion and 2-D resonance frequencies. Geophys J Int 2007;168:1261–75.

[6] Roten D, Fäh D, Olsen KB, Giardini D. A comparison of observed and simulated site response in the Rhone valley, Geophys. J Intell 2008;173:958–78.

[7] Havenith HB, Fäh D, Alvarez-Rubio S, Roten D. Response spectra for the deep sediment-filled Rhône valley in the Swiss Alps. Soil Dynam Earthq Eng 2009;29: 17–38. https://doi.org/10.1016/j.soildyn.2008.01.016.

[8] Ermert L, Poggi V, Burjanek J, Fäh D. Fundamental and higher 2-D resonance modes of an Alpine valley. Geophys J Int 2014;198:795–811.

[9] Poggi V, Ermert L, Burjanek J, Michel C, Fäh D. Modal analysis of 2-D sedimentary basin from frequency domain decomposition of ambient vibration array recordings. Geophys J Int 2015;200(1):615–26. https://doi.org/10.1093/gji/ggu420.

[10] Ewald M, Igel H, Hinzen K-G, Scherbaum F. Basin-related effects on ground motion for earthquake scenarios in the Lower Rhine Embayment. Geophys J Int 2006;166 (1):197–212. https://doi.org/10.1111/j.1365-246X.2006.02909.x.

[11] Olsen KB, Day SM, Minster JB, Cui Y, Chourasia A, Faerman M, Moore R, Maechling P, Jordan T. Strong shaking in Los Angeles expected from southern san andreas earthquake. Geophys Res Lett 2006;33(7). https://doi.org/10.1029/2005GL025472.

[12] Moczo P, Kristek J, Bard PY, Stripajová S, Hollender F, Chovanová Z, Kristeková M, Sicilia D. Key structural parameters affecting earthquake ground motion in 2D and 3D sedimentary structures. Bull Earthq Eng 2018;16:2421–50. https://doi.org/10.1007/s10518018-0345-5.

[13] Graves RW. Three-dimensional finite-difference modeling of the San Andreas fault: source parameterization and ground-motion levels. Bull Seismol Soc Am 1998;88: 881–97.

[14] Olsen KB. Site amplification in the Los Angeles basin from three-dimensional modeling of ground motion. Bull Seismol Soc Am 2000;90:S77–94.

[15] Lee S-J, Chen H-W, Huang B-S. Simulations of strong ground motion and 3D amplification effect in the Taipei basin by using a composite grid finite-difference method. Bull Seismol Soc Am 2008;98(3):1229–42. https://doi.org/10.1785/0120060098.

[16] Swisstopo Federal Office for Topography. Geological vector datasets for better subsurface management: geocover V3 map of Raron CN 1288. 2019.

[17] Swisstopo Federal Office for Topography. GK500, Geological map of Switzerland 1: 500000. Compiled by: Geological Institute, University of Bern and Federal Office for Water and Geology; 2005.

[18] Panzera F, D'Amico S, Lupi M, Mauri G, Karyono K, Mazzini A. Lusi hydrothermal structure inferred through ambient vibration measurements. Mar Petrol Geol 2018; 90:116–24. https://doi.org/10.1016/j.marpetgeo.2017.06.017.

[19] Chieppa D, Hobiger M, Fäh D. Ambient vibration analysis on seismic arrays to investigate the properties of the upper crust: an example from Herdern in Switzerland. Geophys J Int 2020:ggaa182. https://doi.org/10.1093/gji/ggaa182.

[20] Rohmer O, Bertrand E, Mercerat ED, Régnier J, Pernoud M, Langlaude P, Alvarez M. Combining borehole log-stratigraphies and ambient vibration data to build a 3D Model of the Lower Var Valley, Nice (France). Eng Geol 2020;270: 105588. https://doi.org/10.1016/j.enggeo.2020.105588.

[21] Hobiger M, Bergamo P, Imperatori W, Panzera F, Lontsi AM, Perron V, Michel C, Burjánek J, Fäh D. Site characterization of Swiss strong-motion stations: the benefit of advanced processing algorithms. Bull Seismol Soc Am 2021. https://doi.org/ 10.1785/0120200316.

[22] Bonnefoy-Claudet S, Kohler A, Cornou C, Wathelet M, Bard PY. Effects of love waves on microtremor H/V ratio. Bull Seismol Soc Am 2008;98:288–300. https:// doi.org/10.1785/0120070063.

[23] Poggi V, Fäh D. Estimating Rayleigh wave particle motion from three-component array analysis of ambient vibrations. Geophys J Int 2010;180:251–67.

[24] Ibs-von Seht M, Wohlenberg J. Microtremor measurements used to map thickness of soft sediments. Bull Seismol Soc Am 1999;89(1):250–9.

[25] Delgado J, López Casado C, Giner J, Estévez A, Cuenca A, Molina S. Microtremors as a geophysical exploration tool: applications and limitations. Pure Appl Geophys 2000;157:1445–62. https://doi.org/10.1007/PL00001128.

[26] Özalaybey S, Zor E, Ergintav S, Tapırdamaz MC. Investigation of 3-D basin structures in the İzmit Bay area (Turkey) by single-station microtremor and gravimetric methods. Geophys J Int 2011;186(2):883–94. https://doi.org/ 10.1111/j.1365-246X.2011.05085.x.

[27] Molnar S, Cassidy JF, Castellaro S, Cornou C, Crow H, Hunter JA, Matsushima S, Sanchez-Sesma FJ, Yong A. Application of microtremor horizontal-to-vertical spectral ratio (MHVSR) analysis for site characterization: state of the art. Surv Geophys 2018;39(4):613–31.

[28] Satoh T, Kawase H, Matsushima SI. Differences between site characteristics obtained from microtremors, S-waves, P-waves, and codas. Bull Seismol Soc Am 2001;91(2):313–34.

[29] Fäh D, Moore J, Burjanek J, Iosifescu I, Dalguer L, Dupray F, Michel C, Woessner J, Villiger A, Laue J, Marschall I, Gischig V, Loew S, Marin A, Gassner G, Alvarez S, Balderer W, Kästli P, Giardini D, Iosifescu C, Hurni L, Lestuzzi P, Karbassi A, Baumann C, Geiger A, Ferrari A, Laloui L, Clinton J, Deichmann N. Coupled seismogenic geohazards in alpine regions. Bollet Geofisic Teor Appl 2012;53(4): 485–508.

[30] Bergamo P, Hammer C, Fäh D. On the relation between empirical amplification and proxies measured at Swiss and Japanese stations: systematic regression analysis and neural network prediction of amplification. Bull Seismol Soc Am 2021;111(1): 101–20.

[31] Panzera F, Bergamo P, Fäh D. Canonical correlation analysis based on site-response proxies to predict site-specific amplification functions in Switzerland. Bull Seismol Soc Am 2021. https://doi.org/10.1785/0120200326. 2021.

[32] Stutenbecker L, Costa A, Schlunegger F. Lithological control on the landscape form of the upper Rhône basin, central Swiss Alps. Earth Surf Dyn 2016;4:253–72. https://doi.org/10.5194/esurf-4-253-2016.

[33] Schmid SM, Fügenschuh B, Kissling E, Schuster R. Tectonic map and overall architecture of the Alpine orogen. Eclogae Geol Helv 2004;97:93–117.

[34] Egli D, Mancktelow N. The structural history of the Mont Blanc massif with regard to models for its recent exhumation. Swiss J Geosci 2013;106:469–89.

[35] Besson O, Marchant R, Pugin A, Rouiller JD. Campagne de sismique-reflexion dans la vallee du Rhône entre Sion et St. Maurice: perspectives d'exploitation geothermique des depots torrentiels sousglaciaires. Bull Cent d'hydrogeol l'Univ Neuchatel 1993;12:39–58.

[36] Pfiffner OA, Heitzmann S, Mueller S, Steck A. Incision and backfilling of alpine valleys: pliocene, pleistocene and holocene processes. Birkhäuser, Basel: Deep Structure of the Swiss Alps—results of NRP; 1997. p. 265–76.

[37] Rosselli A, Olivier R. Modélisation gravimètrique 2.5D et cartes des isohypses au l: l00000 du substratum rocheux de la Vallée du Rhône entre Villeneuve et Brig (Suisse). Eclogae Geol Helv 2003;96:399–423. https://doi.org/10.1007/s00015-003-1088-z.

[38] Stutenbecker L, Delunela R, Schlunegger F, Silva TA, Šegvićch B, Girardclos S, Bakker M, Costa A, Lane SN, Loizeau JL, Molnar P, Akçar N, Christl M. Reduced sediment supply in a fast eroding landscape? A multi-proxy sediment budget of the upper Rhône basin, Central Alps. Sediment Geol 2018;375:105–19. https://doi. org/10.1016/j.sedgeo.2017.12.013.

[39] Brandolini F, Reynard E, Pelfini M. Multi-temporal mapping of the upper Rhone valley (Valais, Switzerland): fluvial landscape changes at the end of the little ice age (18th–19th centuries). J Maps 2020;16(2):212–21. https://doi.org/10.1080/ 17445647.2020.1724837.

[40] Volker S, Preisig G, Gaehwile M. GeoQuat: developing a system for the sustainable management, 3D modelling and application of Quaternary deposit data. Swiss Bull Angew Geol 2016;21/1:3–16. https://doi.org/10.5169/seals-658182.

[41] Michel C, Fäh D, Edwards B, Cauzzi C. Site amplification at the city scale in Basel (Switzerland) from geophysical site characterization and spectral modelling of recorded earthquakes. Phys Chem Earth, Parts A/B/C 2017;98:27–40. https://doi. org/10.1016/j.pce.2016.07.005.

[42] Panzera F, Lombardo G, Imposa S, Grassi S, Gresta S, Catalano S, Romagnoli G, Tortorici G, Pattia F, Di Maio E. Correlation between earthquake damage and seismic site effects: the study case of Lentini and Carlentini, Italy. Eng Geol 2018; 240:149–62. https://doi.org/10.1016/j.enggeo.2018.04.014.

[43] Fäh D, Kind F, Giardini D. A theoretical investigation of average H/V ratios. Geophys J Int 2001;145:535–49.

[44] Stamm G, Fäh D, Poggi V, Löw I. H/V - measurements in the area of Visp and St. Niklaus. Deliverable No. 3.2. Swiss Seismological Service SED/COGEAR/R/001/ 20090301; 2009.

[45] Burjanek J, Gassner-Stamm G, Fäh D. Array - measurements in the area of Visp and st. Niklaus. Deliverable No. 3.1.2. Swiss Seismological ServiceSED/COGEAR/R/ 003/20100226; 2010.

[46] Michel C, Edwards B, Poggi V, Burjanek J, Roten D, Cauzzi C, Fäh D. Assessment of site effects in alpine regions through systematic site characterization of seismic stations. Bull Seismol Soc Am 2014;104:2809–26. https://doi.org/10.1785/ 0120140097.

[47] Konno K, Ohmachi T. Ground motion characteristics estimated from spectral ratio between horizontal and vertical components of microtremor. Bull Seismol Soc Am 1998;88:228–41.

[48] Sesame. Guidelines for the implementation of the H/V spectral ratio technique on ambient vibrations measurements, processing and interpretation, SESAME European research project. WP12 Deliv 2004;D23:12.

[49] Hobiger M, Bard PY, Cornou C, Le Bihan N. Single station determination of Rayleigh wave ellipticity by using the random decrement technique (RayDec). Geophys Res Lett 2009;36:L14303.

[50] Farrugia D, Paolucci E, D'Amico S, Galea P. Inversion of surface wave data for subsurface shear-wave velocity profiles characterized by a thick buried low-velocity layer. Geophys J Int 2016;206:1221–31. https://doi.org/10.1093/gji/ ggw204.

[51] Panzera F, D'Amico S, Colica E, Viccaro M. Ambient vibration measurements to support morphometric analysis of a pyroclastic cone. Bull Volcanol 2019;81:74. https://doi.org/10.1007/s00445-019-1338-1.

[52] Hallo M, Imperatori W, Panzera F, Fäh D. Joint multizonal transdimensional Bayesian inversion of surface wave dispersion and ellipticity curves for local near-surface imaging. Geophys J Int 2021. https://doi.org/10.1093/gji/ggab116.

[53] Wathelet M. An improved neighborhood algorithm: parameter conditions and dynamic scaling. Geophys Res Lett 2008;35:L09301. https://doi.org/10.1029/ 2008GL033256.

[54] Rosselli A. Modelisation gravimetrique bi- et tridimensionelle du substratum rocheux des vallees alpines. PhD thesis. Universite de Lausanne; 2001.

[55] Poggi V. Report on active seismic experiment at the station SVIO. Swiss Seismological Service; 2011. http://stations.seismo.ethz.ch.

[56] Zimmer MA, Prasad M, Mavko G, Nur A. Seismic velocities of unconsolidated sands: Part 1 — pressure trends from 0.1 to 20 MPa. Geophysics 2007;72(1):E1–13. https://doi.org/10.1190/1.2399459.

[57] Bodet L, Jacob X, Tournat V, Mourgues R, Gusev V. Elasticity profile of an unconsolidated granular medium inferred from guided waves: toward acoustic monitoring of analogue models. Tectonophysics 2010;496:99–104. https://doi. org/10.1016/j.tecto.2010.10.004.

[58] Bergamo P, Socco LV. P- and S-wave velocity models of shallow dry sand formations from surface wave multimodal inversion. Geophysics 2016;81(4): R197–209.

[59] Xia J, Miller RD, Park CB, Tian G. Inversion of high frequency surface waves with fundamental and higher modes. J Appl Geophys 2003;52:45–57.

[60] Edwards B, Michel C, Poggi V, Fäh D. Determination of site amplification from regional seismicity: application to the Swiss national seismic networks. Seismol Res Lett 2013;84(4):611–21.

[61] Pickett GR. Acoustic character logs and their applications in formation evaluation. J Petrol Technol 1963;15:650–67.

[62] Gardner GHF, Harris MH. Velocity and attenuation of elastic waves in sands: society of professional well log analysts, transactions. In: 9th annual log symposium; 1968. M1–19.

[63] Guéguen P, Cornou C, Garambois S, et al. On the limitation of the H/V spectral ratio using seismic noise as an exploration tool: application to the grenoble valley (France), a small Apex ratio basin. Pure Appl Geophys 2007;164:115–34. https:// doi.org/10.1007/s00024-006-0151-x. 2007.

[64] Le Roux O, Cornou C, Jongmans D, Schwartz S. 1-D and 2-D resonances in an Alpine valley identified from ambient noise measurements and 3-D modelling. Geophys J Int 2012;191:579–90. https://doi.org/10.1111/j.1365-246X.2012.05635.x. 2012.

[65] Minasny B, McBratney AB, Whelan BM. VESPER version 1.62. NSW: Australian Centre for Precision Agriculture, McMillan Building A05, The University of Sydney; 2005–06. http://www.usyd.edu.au/su/agric/acpa.

[66] Haas TC. Kriging and automated semivariogram modelling within a moving window. Atmos Environ 1990;24A:1759–69.

[67] Breytenbach IJ, Bosch PJA. Application, advantages and limitations of high-density gravimetric surveys compared with three-dimensional geological modelling in dolomite stability investigations. J S Afr Inst Civ Eng 2011;53(2):7–13.

[68] Petersson NA, Sjögreen B. SW4, version 2.01 [software]. Comput Infrastruct Geodyn 2017. https://doi.org/10.5281/zenodo.1063644. url: https://doi.org/10. 5281/zenodo.1063644.

[69] Petersson NA, Sjögreen B. User's guide to SW4, version 2.0, LLNL-SM-741439 (LLNL-SM-741439). 2017.

[70] Petersson NA, Sjögreen B. Super-grid modeling of the elastic wave equation in semi-bounded domains. Commun Comput Phys 2014;16:913–55.

[71] Lunedei E, Malischewsky P. A review and some new issues on the theory of the H/V technique for ambient vibrations. In: Ansal A, editor. Perspectives on European earthquake engineering and seismology. Geotechnical, geological and earthquake engineering, vol. 39. Cham: Springer; 2015. https://doi.org/10.1007/978-3-319-16964-4_15.

[72] Borcherdt RD. Effects of local geology on ground motion near San Francisco Bay. Bull Seismol Soc Am 1970;60:29–61.

[73] Burjanek J, Gassner-Stamm G, Poggi V, Fäh D. Estimation of local site effects in the Upper Valais (Switzerland). In: 4th IASPEI/IAEE international symposium: effects

of surface geology on seismic motion august 23–26, 2011. University of California Santa Barbara; 2011.

[74] Steidl JH, Tumarkin AG, Archuleta RJ. What is a reference site? Bull Seismol Soc Am 1996;86:1733–48.

[75] Rösler B, van der Lee S. Using seismic source parameters to model frequency-dependent surface-wave radiation patterns. Seismol Res Lett 2020;91:992–1002.

[76] Zeng Y, Anderson JG, Yu G. A composite source model for computing realistic synthetics strong ground motions. Geophys Res Lett 1994;21:725–8.

[77] Zeng Y, Anderson JG, Su F. Subevent rake and random scattering effects in realistic strong ground motion simulation. Geophys Res Lett 1995;22:17–20. https://doi.org/10.1029/94GL02798.